The Astrophysical Journal, 945:126 (18pp), 2023 March 10 https://doi.org/10.3847/1538-4357/acb68b

First Observations of the Brown Dwarf HD 19467 B with JWST

Alexandra Z. Greenbaum[1], Jorge Llop-Sayson[2], Ben W.P. Lew[3,15], Geoffrey Bryden[4], Thomas L. Roellig[3], Marie Ygouf[4], B. J. Fulton[5], Daniel R. Hey[6], Daniel Huber[6], Sagnick Mukherjee[7], Michael Meyer[8], Jarron Leisenring[9], Marcia Rieke[9], Martha Boyer[10], Joseph J. Green[4], Doug Kelly[9], Karl Misselt[9], Eugene Serabyn[4], John Stansberry[10], Laurie E. U. Chu[11], Matthew De Furio[8], Doug Johnstone[12,13], Joshua E. Schlieder[14], and Charles Beichman[4,5]

[1] IPAC, California Institute of Technology, 1200 E. California Boulevard, Pasadena, CA, 91125, USA; azg@ipac.caltech.edu
[2] Department of Astronomy, California Institute of Technology, 1200 E. California Boulevard, Pasadena, CA, 91125, USA
[3] NASA Ames Research Center, Mountain View, CA, 94035, USA
[4] Jet Propulsion Laboratory, California Institute of Technology, Pasadena, CA, 91109, USA
[5] NASA Exoplanet Science Institute, Caltech-IPAC, 1200 E. California Boulevard, Pasadena, CA, 91125, USA
[6] Institute for Astronomy, University of Hawai'i, 2680 Woodlawn Drive, Honolulu, HI, 96822, USA
[7] Department of Astronomy and Astrophysics, University of California, Santa Cruz, CA, 95064, USA
[8] Department of Astronomy, University of Michigan, Ann Arbor, MI, 48109, USA
[9] Steward Observatory, University of Arizona, Tucson, AZ, 85721, USA
[10] Space Telescope Science Institute, 3700 San Martin Drive, Baltimore, MD, 21218, USA
[11] NASA Postdoctoral Program Fellow, NASA Ames Research Center, M/S 245-1, Moffett Field, CA, 94035, USA
[12] NRC Herzberg Astronomy and Astrophysics, 5071 West Saanich Road, Victoria, BC, V9E 2E7, Canada
[13] Department of Physics and Astronomy, University of Victoria, Victoria, BC, V8P 5C2, Canada
[14] Exoplanets and Stellar Astrophysics Laboratory, NASA Goddard Space Flight Center, 8800 Greenbelt Road, Greenbelt, MD, USA
[15] Bay Area Environmental Research Institute, P.O. Box 25, Moffett Field, CA, 94035, USA
Received 2022 November 17; revised 2023 January 25; accepted 2023 January 25; published 2023 March 14

Abstract

We observed HD 19467 B with JWST's NIRCam in six filters spanning 2.5–4.6 μm with the long-wavelength bar coronagraph. The brown dwarf HD 19467 B was initially identified through a long-period trend in the radial velocity of the G3V star HD 19467. HD 19467 B was subsequently detected via coronagraphic imaging and spectroscopy, and characterized as a late-T type brown dwarf with an approximate temperature ~1000 K. We observed HD 19467 B as a part of the NIRCam GTO science program, demonstrating the first use of the NIRCam Long Wavelength Bar coronagraphic mask. The object was detected in all six filters (contrast levels of 2×10^{-4} to 2×10^{-5}) at a separation of 1.″6 using angular differential imaging and synthetic reference differential imaging. Due to a guide star failure during the acquisition of a preselected reference star, no reference star data were available for post-processing. However, reference differential imaging was successfully applied using synthetic point-spread functions developed from contemporaneous maps of the telescope's optical configuration. Additional radial velocity data (from Keck/HIRES) are used to constrain the orbit of HD 19467 B. Photometric data from TESS are used to constrain the properties of the host star, particularly its age. NIRCam photometry, spectra, and photometry from the literature, and improved stellar parameters are used in conjunction with recent spectral and evolutionary substellar models to derive the physical properties of HD 19467 B. Using an age of 9.4 ± 0.9 Gyr inferred from spectroscopy, Gaia astrometry, and TESS asteroseismology, we obtain a model-derived mass of $62 \pm 1\ M_J$, which is consistent within 2σ with the dynamically derived mass of $81^{+14}_{-12}\ M_J$.

Unified Astronomy Thesaurus concepts: Brown dwarfs (185); Coronagraphic imaging (313); High contrast techniques (2369)

1. Introduction

Brown dwarfs provide a unique testbed for confronting evolutionary and atmospheric models of substellar objects with well-defined observations. Those brown dwarfs which are companions to main-sequence stars, as opposed to free-floating, are particularly valuable since they are presumed to inherit observable stellar properties such as metallicity and share similar ages. This knowledge constrains many of the free parameters in the comparison of models with observation.

Low-mass brown dwarf companions to main-sequence stars were initially found through blind imaging searches, e.g., GL229 B (Nakajima et al. 1995), and subsequently as a by-product of planet searches using the radial velocity (RV) technique. In the case of HD 19467, Crepp et al. (2014) identified it as a star with a significant RV trend suggestive of a massive brown dwarf companion. Coronagraphic imaging with Keck NIRC2 first confirmed the presence of the companion (Crepp et al. 2014). This was followed by spectroscopy with Palomar's P1640 instrument that characterized HD 19467 B as a brown dwarf with an effective temperature of ~1000 K, corresponding to a T5.5 spectral type (Crepp et al. 2015). More recently, proper motion measurements from the Hipparcos and Gaia catalogs have been used to identify systems with companions or help characterize them, including HD 19467 (Brandt et al. 2021a).

Multiple JWST programs will provide imaging and spectroscopy of HD 19467 B across the near- and mid-IR where brown dwarfs emit most of their energy. The program presented here (PID #1189) uses NIRCam (M. Rieke et al.

Table 1
NIRCam Observing Parameters (PID:#1189)

Target	Filter	Readout	Groups/Int	Ints/Exp	Dithers	Exp Time (s)
Subarray SUB320; Roll 1						
HD 19467	F250M	MEDIUM2	10	10	1	983.517
HD 19467	F300M	MEDIUM2	10	5	1	491.758
HD 19467	F360M	MEDIUM2	10	5	1	491.758
HD 19467	F410M	MEDIUM2	10	5	1	491.758
HD 19467	F430M	MEDIUM2	10	5	1	491.758
HD 19467	F460M	MEDIUM2	10	5	1	491.758
Subarray SUB320; Roll 2						
HD 19467	F250M	MEDIUM2	10	10	1	983.517
HD 19467	F300M	MEDIUM2	10	5	1	491.758
HD 19467	F360M	MEDIUM2	10	5	1	491.758
HD 19467	F410M	MEDIUM2	10	5	1	491.758
HD 19467	F430M	MEDIUM2	10	5	1	491.758
HD 19467	F460M	MEDIUM2	10	5	1	491.758

Note. Observations of reference star HD 19096 were not executed. The exposure time refers to the effective exposure time reported in the data headers, keyword XPOSURE.

2023, in press) to provide medium- and narrow-band imaging and photometry of HD 19467 B in six bands, spanning 2.5–4.5 μm. At a later date, another JWST program (PID #1414) will use NIRSpec (Jakobsen et al. 2022) to obtain high-resolution ($R \simeq 2700$) 3–5 μm spectra of HD 19467 B.

JWST observations of the G3V star HD 19467 with its T5+ brown dwarf companion, HD 19467 B (Crepp et al. 2014), represent one of the earliest exercises of the NIRCam Coronagraphic LW Bar (Krist et al. 2007; Beichman et al. 2010; Girard et al. 2022), providing an opportunity for an early scientific result and a demonstration of the capabilities of the instrument.

The NIRCam observations presented in this study are designed to accomplish three main goals:

1. Provide an early data set that exercises the bar mask on NIRCam, especially without a reference star (Sections 2 and 4);
2. Refine the orbital parameters of HD 19467 B with a new imaging data point along with new RV data from Keck/HIRES (Section 5); and
3. Add additional photometric measurements to constrain the physical properties of the brown dwarf better (Section 6).

We also include new analysis of TESS observations to constrain the properties of the host star (Section 3).

2. Observations

2.1. NIRCam Observations

NIRCam observed HD 19467 on 2022 August 12 with the long-wavelength bar (LWB) coronagraphic mask in subarray mode with six filters: F250M, F300M, F360M, F410M, F430M, and F460M. The target star was observed at two telescope roll angles separated by 7°.72. Table 1 shows a summary of the observations and settings per filter. Observations of HD 19467 were taken with the long-wavelength bar coronagraph mask (MASKLWB), providing a test of NIRCam's capabilities at smaller inner working angles than are possible with the round masks ($4\lambda/D$ for MASKLWB versus $6\lambda/D$ for MASK210R, MASK335R, and MASK430R; Krist et al. 2007). At the time of these observations, the MASKLWB positions were not well-defined, with a y-offset ~70 mas. Future use of this mode with an updated position definition will improve the ability to center the star on the mask and therefore contrast performance, especially close in to the mask. These observations represent one of the first post-commissioning uses of the bar coronagraph.

The observation plan was initially scheduled to include sequential observations of the reference star HD 19096 in order to perform point-spread function (PSF) subtraction using reference differential imaging (RDI). However, the reference observations were unsuccessful because the telescope failed to acquire a guide star. Instead, we performed post-processing using only angular diversity along with models of the telescope's and instrument's optical performance enabled by regular measurements of the telescope wave front error, simulating reference star differential imaging but without the actual observation of a reference star. A very similar approach has been applied to enable high-contrast imaging with the Hubble Space Telescope by modeling the instrumental PSF (e.g., Krist et al. 1997); JWST's stability and regular measurements of the wave front further enable this technique. High-contrast observations with only angular diversity can significantly reduce the observation time and overhead. We demonstrate that this can be an appropriate strategy for bright and widely separated companions.

2.2. RV Observations

New RV measurements of HD 19467 were obtained in 2022 July through 2022 August using the High Resolution Echelle Spectrometer (HIRES) on the Keck I Telescope. The new RV measurements are processed using standard data reduction techniques described in Butler et al. (1996) and Butler et al. (2017). The majority of the RVs come from Rosenthal et al. (2021), where the reduction techniques are described in more detail. In brief, the HIRES RV values are measured using an iodine cell-based design in order to calibrate the wavelengths in the stellar spectrum. The spectral region from 5000 to 6200 Å is used for measuring the RVs. We combine the new observations with previous measurements for a total of 53

Table 2
Observations of the Host Star HD 19467

Property	Value	Units	Comments
Spectral Type	G3V		Gomes da Silva et al. (2021)
$T_{\rm eff}$	5720 ± 10	K	Gomes da Silva et al. (2021)
$T_{\rm eff}$	5747 ± 25	K	Brewer et al. (2016)
$T_{\rm eff}$	5770 ± 80	K	Maire et al. (2020)
$T_{\rm eff}$	5742 ± 10	K	Nissen et al. (2020)
Mass	0.953 ± 0.022	$M_\odot$	Maire et al. (2020)
Mass	0.960 ± 0.02	$M_\odot$	This work (Section 3.2)
Age	$5.41^{+1.8}_{-1.34}$	Gyr	Brandt et al. (2021a)
Age	$8.0^{+2.0}_{-1.0}$	Gyr	Maire et al. (2020, Table 1)
Age	$10.06^{+1.16}_{-0.82}$	Gyr	Wood et al. (2019)
Age	11.882 ± 2.564	Gyr	Gomes da Silva et al. (2021)
Age	9.4 ± 1.0	Gyr	This work (Section 3.3)
[Fe/H]	-0.11 ± 0.01	dex	Maire et al. (2020)
[Fe/H]	-0.09 ± 0.04	dex	This work (Section 3.2)
log(g)	4.32 ± 0.06	cgs	Maire et al. (2020)
log(g)	4.28 ± 0.04	cgs	This work (Section 3.2)
R.A. (Eq 2000; Ep 2000)	$03^{\rm h}07^{\rm m}18\overset{\rm s}{.}570$		Gaia DR3
Decl.. (Eq 2000; Ep 2000)	$-13°45'42\overset{''}{.}419$		Gaia DR3
Distance	32.03 ± 0.03	pc	Gaia DR3
Proper Motion (μ_α, μ_δ)	$(-8.694, -240.64)$	mas/yr	Gaia DR3
RUWE	1.0566		Gaia DR3
G	6.814 ± 0.003	mag	Gaia DR3
H	5.447 ± 0.033	mag	2MASS
W1 [3.4 μm]	5.36 ± 0.16	mag	WISE
W2 [4.6 μm]	5.18 ± 0.06	mag	WISE

RV measurements spanning 25 yr for the data analysis. The data including the new measurements are listed in Table 8 in Appendix B.

2.3. TESS Observations

HD 19467 was observed by the TESS spacecraft (Ricker et al. 2015) in Sectors 4 and 31, resulting in ≈60 days of high-precision optical photometry. Sector 31 includes data obtained with a 20 s cadence, a new observing mode introduced in the TESS extended mission. The TESS 20 s data show improved photometric precision for bright stars such as HD 19467 (Huber et al. 2022), and we therefore focus on the 20 s data here. We used the PDC-MAP light curves provided by the Science Processing Operations Center (SPOC; Jenkins et al. 2016), which have been optimized to remove instrumental variability (Smith et al. 2012; Stumpe et al. 2012), and remove all data with quality flags not equal to zero, which yields the best precision of the 20 s data (Huber et al. 2022).

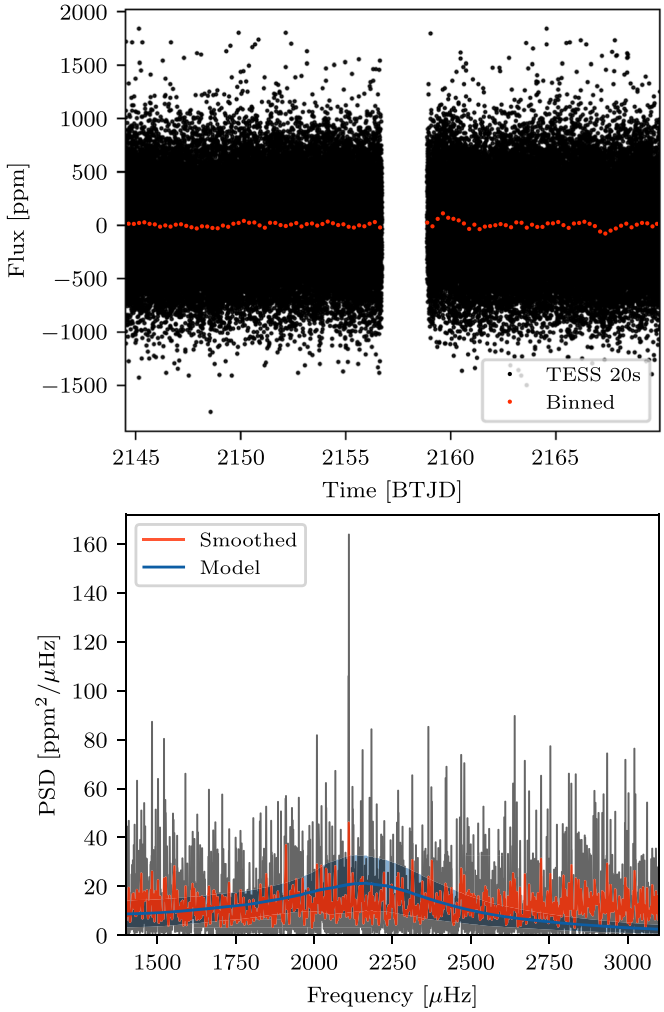

Figure 1. Top: TESS Sector 31 light curve of HD 19467. The black points show the original 20 s cadence data and the red points show the data binned to a timescale of 6 hr. Bottom: power spectrum of the data centered on the detected power excess near ≈2200 μHz. The blue line and filled area show the median and standard deviation of the GP model posterior, respectively.

3. Host Star Properties

HD 19467 is a slightly metal-poor G3 main-sequence star (Gomes da Silva et al. 2021), as summarized in Table 2. In some cases multiple values are given for key parameters to give an idea of their spread. The biggest discrepancy concerns the age estimates, which range from $5.41^{+1.8}_{-1.34}$ to 11.88 ± 2.56 Gyr (Wood et al. 2019; Maire et al. 2020; Brandt et al. 2021a; Gomes da Silva et al. 2021). Maire et al. (2020) apply different approaches to age determination and provide a thorough discussion of their merits and drawbacks. Their work generally suggests older ages than the initial Crepp et al. (2014) estimation but they note that the chemical abundance and kinematics likely place HD 19467 in the thin-disk population, suggesting an age younger than 10 Gyr. We discuss our choice of age in more detail below, including new asteroseismology data from TESS, which favor an older age.

3.1. Analysis of TESS Photometry

The top panel of Figure 1 shows the TESS 20 s cadence light curve for HD 19467. We observe no significant long-term variability, with an rms of 25.5 ppm over 6 hr timescales. To

search for high-frequency variability, we used the established asteroseismic tools pySYD (Huber et al. 2009; Chontos et al. 2021) and FAMED (Corsaro et al. 2020), which analyze the data in the frequency domain. Both methods detected a significant power excess near ≈2200 μHz, consistent with the expected ≈7 minute timescale of solar-like oscillations (Bedding 2014; García & Ballot 2019) based on the spectroscopic temperature and surface gravity (Table 2). We also analyzed the data in the time-domain using a Gaussian process (GP) model with a stochastically driven damped harmonic oscillator (Foreman-Mackey et al. 2017), which has been demonstrated to outperform traditional frequency analysis tools in recovering low signal-to-noise (S/N) oscillations (D. R. Hey et al. 2023, in preparation). The GP analysis strongly favored a model with an oscillating component with a Bayesian information criterion (BIC) of $\Delta\mathrm{BIC} = 7.1$.

The bottom panel of Figure 1 shows a power spectrum of the 20 s light curve centered on the power excess. Solar-like oscillations are described by a frequency of maximum power (ν_{max}) and a large frequency separation ($\Delta\nu$), which approximately scale with $\log g$ and the mean stellar density, respectively (Ulrich 1986; Brown et al. 1991). We derive $\nu_{\mathrm{max}} = 2180 \pm 100$ μHz, with the central value taken from the median of three solutions (pySYD, FAMED, and GP), and uncertainties calculated from the scatter over individual methods (e.g., Huber et al. 2013). The low S/N of the detection precludes an unambiguous detection of $\Delta\nu$. Visual inspection of the echelle diagram indicates $\Delta\nu \approx 101$ μHz, consistent with the derived ν_{max} value.

3.2. Physical Properties of HD 19467

We adopted the effective temperature (T_{eff}) and metallicity ([M/H]) from Brewer et al. (2016), derived from a line-by-line analysis of a Keck/HIRES spectrum. Literature values from spectroscopy and Gaia color–temperature relations (Casagrande et al. 2021) are highly consistent, with a range of 40 K in T_{eff} and 0.04 dex in iron abundance (Table 2). We used these ranges as estimates for the uncertainties, resulting in $T_{\mathrm{eff}} = 5747 \pm 40$ K and $[\mathrm{M/H}] = -0.09 \pm 0.04$ dex. These uncertainties are smaller than those recommended by Tayar et al. (2022), which are justified by the fact that the star has properties similar to the Sun and thus suffers from smaller systematic errors.

We then combined the asteroseismic ν_{max} measurement, Gaia DR3 parallax, 2MASS K-band magnitude, T_{eff}, and [M/H] with isoclassify (Huber et al. 2017) and BASTA (Aguirre Børsen-Koch et al. 2022), which perform Bayesian inference of stellar parameters given input observables using the stellar evolution models MIST (Choi et al. 2016) and BASTI (Pietrinferni et al. 2004), respectively. Importantly, ν_{max} tightly constrains the surface gravity to $\log g = 4.28$, which combined with the radius constraint from the Gaia parallax provides a tight constraint on its stellar mass, which in turn constrains its stellar age. Both tools consistently imply a mass of ≈0.95 $M_{\odot}$, which, given that the star has slightly evolved off the main sequence (1.2 $R_{\odot}$), implies an old age. Figure 2 shows the age posteriors from both evolutionary models and methods.

The final stellar parameters adopted in our study are listed in Table 3. We adopt the self-consistent solution derived from isoclassify, but add in quadrature the difference to the BASTA results to account for systematic errors due to different model grids (Tayar et al. 2022).

3.3. The Age of HD 19467

The age of HD 19467 is important for interpreting the mass and atmospheric composition of the brown dwarf companion. As already mentioned, literature estimates have a significant spread, ranging from 5 to 12 Gyr (Table 3). Younger, Sun-like ages come from stellar rotation (Maire et al. 2020) and activity (Brandt et al. 2021a), while older ages are preferred by isochrone fitting (Wood et al. 2019; Maire et al. 2020). The rotation-age is based on the detection of a photometric period of ≈29 days with an amplitude of ≈0.5% from ground-based ASAS data (Maire et al. 2020). The high-precision of the TESS light curve in Figure 1 rules out rotational modulation at the level of 0.5% over the 29 day timescale suggested by the ASAS data, which implies that the rotation period for HD 19467 is undetermined. This is consistent with results from the Kepler Mission, which demonstrated that typical rotational amplitudes in mature Sun-like stars are on the order of a few hundred ppm (McQuillan et al. 2014; Santos et al. 2021) and thus are generally not detectable using ground-based photometry. Chromospheric activity-based ages also become more challenging for stars with Sun-like and older ages due flattening of the age–activity relation, making age constraints sensitive to small changes in R'_{HK} measurements. While some literature values for R'_{HK} favor near-solar values (and thus ages) for HD 19467, others are consistent with older, isochrone-based ages (e.g., $R'_{\mathrm{HK}} = 5.1$ and 8.8 ± 0.3 Gyr; Lorenzo-Oliveira et al. 2018).

The asteroseismic detection from TESS supports an older age for HD 19467. While the low S/N precludes a direct age from a measurement of individual oscillation frequencies (e.g., Mathur et al. 2012; Metcalfe et al. 2014; Silva Aguirre et al. 2017), the ν_{max} measurement precisely constrains $\log g$ and thus stellar mass independent of stellar evolutionary models. With a mass similar to solar (0.96 ± 0.02 $M_{\odot}$), HD 19467 must have an age significantly older than the Sun to reach a radius of 1.2 $R_{\odot}$.[16] As discussed by Maire et al. (2020), an age of 9.4 ± 1.0 Gyr is compatible with the slight enhancements in alpha elements and subsolar metallicity, placing the star in the transition region between chemical "thin-disk" and "thick-disk" stars. Overall, we conclude that HD 19467 is an ≈4–5 Gyr older analog to our Sun and adopt an age of 9.4 ± 1.0 Gyr (Table 3).

4. NIRCam Data Reduction and Post-processing

We use the processed images retrieved from the Mikulski Archive for Space Telescopes (MAST)[17] that have been corrected for bad pixels, flat-fielding, and background subtraction with the jwst pipeline. The product we use are the calints files which result from Stage 2 of the pipeline and have been through a photometric calibration. The data were processed with the calibration software version 1.5.3 and calibration reference data context jwst_0943.pmap. In addition to these data, we take advantage of wave front information provided by optical path difference (OPD) maps taken by the NIRCam wave front sensing team[18] to generate a NIRCam PSF model close in time to our science observations. For synthetic PSFs, we utilize the OPD from 2022 August 11,

[16] This analogy is only slightly affected by the substellar metallicity of HD 19467; a solar-mass star with -0.09 ± 0.04 has an age of ≈3.6 Gyr at solar radius.

[17] https://mast.stsci.edu/

[18] https://webbpsf.readthedocs.io/en/latest/available_opds.html

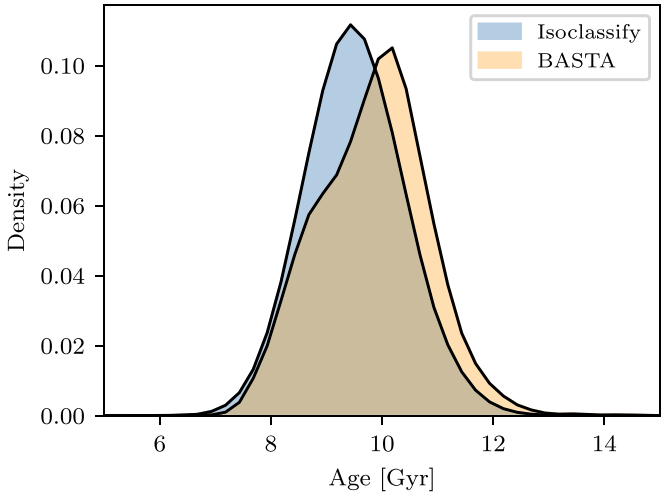

Figure 2. Posterior distributions for the age of HD 19467 based on isochrone modeling with `isoclassify` (blue) and BASTA (orange) using constraints from asteroseismology, spectroscopy, and Gaia data.

Table 3
Adopted Stellar Parameters for HD 19467A

Effective temperature, $T_{\rm eff}$ (K)	5747 ± 40
Metallicity, [M/H] (dex)	-0.09 ± 0.04
Luminosity, L ($L_\odot$)	1.42 ± 0.06
Stellar radius, $R_\star$ ($R_\odot$)	1.20 ± 0.03
Stellar mass, $M_\star$ ($M_\odot$)	0.96 ± 0.02
Stellar density, $\rho_\star$ (cgs)	0.56 ± 0.03
Surface gravity, $\log g$ (cgs)	4.28 ± 0.04
Age, t (Gyr)	9.4 ± 1.0

Note. $T_{\rm eff}$ and [M/H] are adopted from Brewer et al. (2016), with uncertainties accounting for the spread in literature results. All other properties are derived from the combination of constraints from asteroseismology, spectroscopy, and Gaia data (see Section 3).

R2022081102-NRCA3_FP1-1.fits, the closest in time preceding our observations.

4.1. PSF Subtraction

We apply principal component analysis (PCA; e.g., Lafreniere et al. 2007; Amara & Quanz 2012) via Karhunen Loéve Image Projection (KLIP; Soummer et al. 2012), to subtract the residual stellar intensity from the science frames using the images taken at two roll angles for angular diversity. We perform PSF subtraction using the open source Python package `pyKLIP` (Wang et al. 2015) using angular differential imaging (ADI) and RDI using a synthetic reference PSF, as described below. The results of the PCA reduction for all filters are displayed in Figure 3.

For all filters except F250M, the data contained in the two rolls suffice to obtain an unambiguous detection of the companion. For the F250M case, although the companion's signal is visible using only ADI, we resorted to using RDI with a set of synthetic PSFs in order to confirm that the signal is indeed from the companion and not due to residual speckles. In Figure 4 we show a comparison, for the F250M filter, between only using the roll frames for the PCA reduction (ADI), and assisting the PCA reduction with a set of synthetic PSFs (ADI +SynRDI).

A grid of synthetic stellar PSFs is generated using `WebbPSF` (Perrin et al. 2014) and tools from `webbpsf_ext`[19] at offset locations with respect to the coronagraph focal plane mask. We generate simulated PSFs in different sets of 9-point grid patterns at even spacings. We simulate spacings of 2.5, 7, 15, 25, and 40 mas, in addition to a set of rotations of the coronagraphic-PSF with respect to the detector of $0\overset{\circ}{.}1$, $0\overset{\circ}{.}3$, and $0\overset{\circ}{.}5$. This aims to emulate the speckles present in the data frames, and assists the PCA reduction with the diversity in speckle structure needed to perform a more optimal reference subtraction.

As mentioned above, for filters F300M, F360M, F410M, F430M, and F460M, ADI suffices for a clear detection. As a second step we use RDI with the synthetic PSFs to subtract the unwanted starlight further. This is motivated by the fact that the companion PSF's northern lobe falls near the diffraction speckles caused by the bar coronagraph. The number of KL modes determines how many of the synthetic PSFs are used for the subtraction. Since these have been generated with arbitrary offsets, there is a risk of subtracting light from the secondary. We use 15 KL modes, which minimizes over-subtraction and clears out slightly more of the residual starlight around the northern lobe. This was done by visual inspection; a more in-depth analysis on how to use synthetic PSFs optimally will be explored in the future.

4.2. Photometry

To extract the flux and position of HD 19467 B accurately, we account for over-subtraction effects on the PSF that arise during the reduction process (described in Section 4.1) with a forward model based on the method described by Pueyo (2016). We make use of its implementation on `pyKLIP` (Wang et al. 2015). The companion PSF is modeled using `WebbPSF` (Oschmann et al. 2014) for each filter and accounting for its position with respect to the bar focal plane mask. An accurate position of the simulated PSF is particularly important in the case of the shorter wavelength filters: poorer spatial sampling of the pixels compared to the diffraction limit at smaller wavelengths (2.5 μm is sub-Nyquist) results in an acute sensitivity of the PSF structure as seen in the detector. Accurate positioning for the case of F250M was done by trial and error simulating a grid of PSF offsets and selecting the best fit by the least-squares difference between the simulated and the coadded science frames. The model PSFs are simulated using the OPD map closest in time and prior to the observations.

The flux and position of the companion are extracted with `pyKLIP`. We fit a model of its photometry and astrometry to the reduced data using an Markov Chain Monte Carlo (MCMC) approach (`emcee`; Foreman-Mackey et al. 2013). Figure 5 shows the PSF model fit to the reduced data for F360M, the filter in which we obtain the highest S/N. Appendix A contains the full gallery of forward-model comparisons with the PSF-subtracted images in each band.

The flux calibration of the signal is determined based on a `jwst` stage 2 pipeline photometric calibration. We apply a flux correction to the photometry based on a measured attenuation factor of 0.92 of the bar mask Lyot stop at $\sim 1\overset{''}{.}6$. We fit a G3V stellar photosphere model to 1–5 μm photometry from 2MASS (Cutri et al. 2003) and WISE (Cutri et al. 2012). We also find a $\sim$2% error in fitting the stellar model to the IR measurements,

[19] https://github.com/JarronL/webbpsf_ext

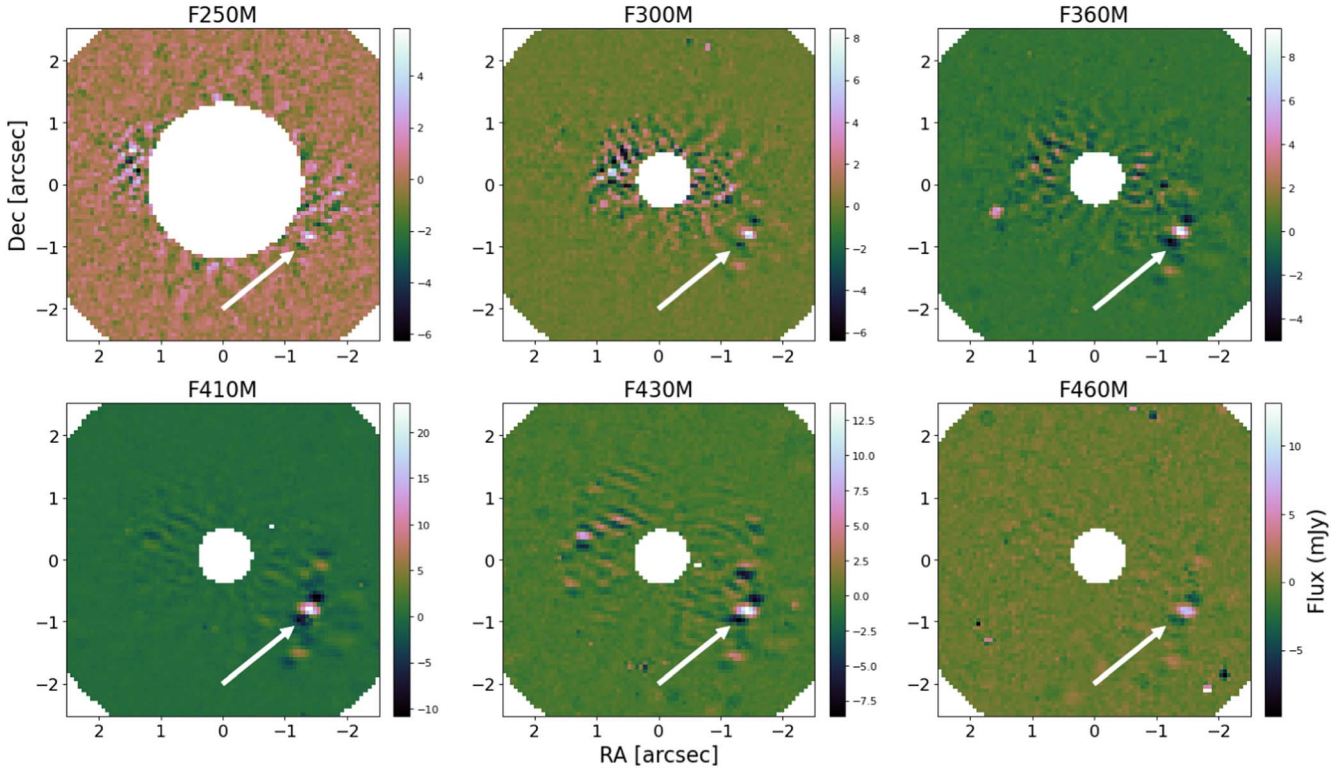

Figure 3. Post-processed images of HD 19467 in the six NIRCam filters observed in this program, rotated so that North is up. Images were reduced using the `pyKLIP` algorithm as described in the text. Arrows indicate the detected companion.

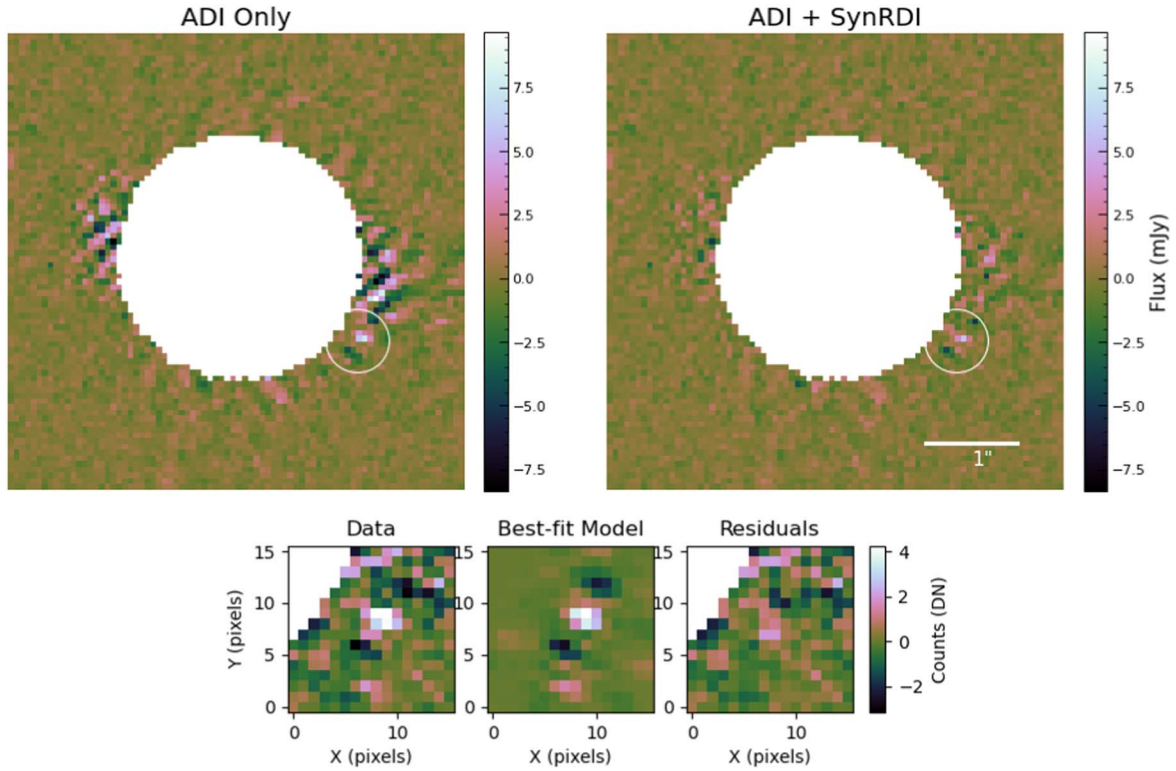

Figure 4. Top: comparison between using only ADI for the PCA reduction (left), and using RDI with synthetic PSFs generated with `WebbPSF` (right) for the the F250M data. The addition of RDI reduces the speckle noise in the PSF-subtracted images. The data are oriented so that North is up. Bottom: the forward model compared with the PSF-subtracted data for F250M, using the sythetic PSFs as reference.

and apply this error to contrast the reported values. Table 4 shows the estimated stellar flux. Comparison of the calibrated flux measured from the acquisition and astrometric confirmation images, both taken through the neutral density square, produced from the stage 2 pipeline is consistent with the estimated stellar spectrum within ∼10%. We therefore

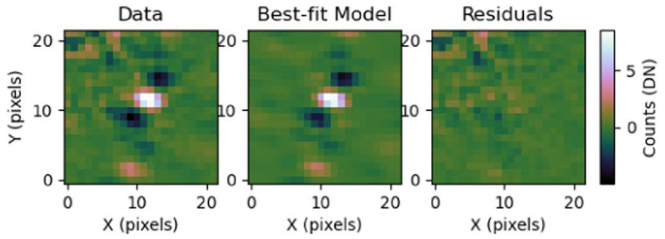

Figure 5. The best-fit model to the PSF-subtracted signal used to measure the photometry and astrometry of HD 19467 B in F360M, where the highest S/N was achieved. The residuals show the companion is fit well by the forward model.

Table 4
Adopted Photometry For HD 19467 B

Filter	Flux (Jy)
F250M flux (Jy)	3.51 ± 0.07
F300M flux (Jy)	2.63 ± 0.05
F335M flux (Jy)	2.10 ± 0.04
F360M flux (Jy)	1.82 ± 0.04
F410M flux (Jy)	1.49 ± 0.03
F430M flux (Jy)	1.36 ± 0.03
F460M flux (Jy)	1.12 ± 0.02

Note. Predicted fluxes in the JWST wavebands are based on BOSZ stellar models (Bohlin et al. 2017).

apply a 10% uncertainty to the reported absolute photometry of HD 19467 B in this section.

Figure 6 shows the measured photometry in each NIRCam band alongside recent measurements and limits from the ground (Maire et al. 2020; Mesa et al. 2020). The F460M flux is consistent with the *M*-band upper limit obtained with the Very Large Telescope (VLT) Nasmyth Adaptive Optics System Near-Infrared Imager and Spectrograph (NACO; Maire et al. 2020), however there appears to be some tension with the NACO *L*' flux compared with the F360M and F410M photometry measurements. The difference in passbands on a steeply rising part of the spectrum, possible water vapor effects, as well as calibration uncertainties may account for this discrepancy. Continued refinement of JWST's photometric calibrations will help identify any biases in the photometry. For this study, we do not incorporate NACO photometry into the analysis, but will rather present a measurement comparison in a future investigation.

Table 5 shows our measured photometry and relative astrometry for HD 19467 B (see the next section).

4.3. Relative Astrometry

A major challenge in obtaining relative astrometry of a companion in coronagraphic imaging is that the primary star is occulted by the focal plane mask. Knowledge of the wave front from published OPD maps and a highly structured PSF enable a forward-model-based cross-correlation with the data to fit for the centroid of the star behind the mask. We perform a cross-correlation of the model PSFs with the data using `chi2_shift` in the `image-registration` Python package[20] to measure the best-fit position of the star behind the mask

[20] https://image-registration.readthedocs.io/

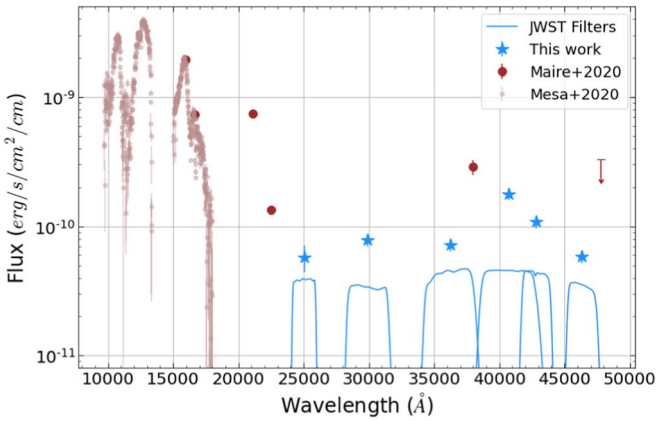

Figure 6. New NIRCam photometry (blue stars) compared with recent ground-based measurements from VLT-SPHERE and VLT-NACO.

(Figure 7). We obtain a centroiding error of ~7 mas, consistent with the measured sensitivity in Carter et al. (2022).

The companion position is recovered with the joint astrometry and photometry model fit to the reduced data as described in Section 4.2. The model fit errors provide the uncertainty in the relative position to the measured star position on the detector. We add the star position uncertainties to the reported errors (Table 5). Figure 8 shows the new astrometric measurement compared to previous relative astrometry measurements of HD 19467 B (Crepp et al. 2014, 2015; Bowler et al. 2020; Maire et al. 2020).

4.4. Performance and Sensitivity

In Figure 9 we show contrast curves for the reduced images after PSF subtraction. The contrast is measured with `PyKLIP` by computing the noise in an azimuthal annulus at each separation, using a Gaussian cross-correlation to remove high-frequency noise. The flux normalization to obtain these contrast numbers was computed as explained in Section 4.2, by using a best-fit model of the stellar spectrum to calibrate the contrast. The contrast curves are corrected for algorithmic throughput, i.e., throughput loss due to the PSF subtraction, and for small sample statistics (Mawet et al. 2014).

Figure 10 translates our detection limits from flux/contrast sensitivities to limits on companion mass. Three different brown dwarf evolution models are considered: Ames-COND (Baraffe et al. 2003), BEX-HELIOS (Linder et al. 2019), and Sonora-Bobcat (Marley et al. 2021). In each case, we assume solar metallicity.

While the shortest wavelength observations achieve the best contrast (in particular F300M), the longer wavelengths are better at detecting lower-mass companions. We find an overall detection limit of ~10 M_J. This limit is much higher than the sub-Jupiter levels that JWST/NIRCam can obtain for young systems (e.g., Carter et al. 2022), but even for this very old system brown dwarfs are easily detectable outside of $\sim 0\farcs4 \simeq$ 10 au. While the detection limit is relatively independent of the model, it does depend significantly on the age of the brown dwarf (the system age is discussed in Section 3.3).

Despite a lack of reference star observations, we are able to recover the signal of HD 19467 B with two roll angles and achieve contrasts of $\sim 10^{-5}$ at 1″–2″. Regular OPD measurements enable the use of synthetic PSFs that can aid PSF subtraction by generating a set of reference PSFs to capture

Table 5
NIRCam measurements of HD 19467 B

Filter	Separation (″)	Pos. Angle (deg)	Δmag (mag)	Flux (μJy)
F250M	1.597 ± 0.010	236.9 ± 0.14	13.67 ± 0.271	11.96 ± 2.75
F300M	1.611 ± 0.002	237.2 ± 0.04	12.62 ± 0.122	23.50 ± 2.52
F360M	1.610 ± 0.003	236.9 ± 0.07	11.91 ± 0.127	31.41 ± 3.58
F410M	1.604 ± 0.001	236.8 ± 0.04	10.45 ± 0.116	98.74 ± 10.20
F430M	1.609 ± 0.003	236.6 ± 0.07	10.78 ± 0.124	66.32 ± 7.35
F460M	1.609 ± 0.003	236.9 ± 0.07	11.07 ± 0.121	41.78 ± 4.64

Note. NIRCam astrometry and photometry from 2022 August 12. The astrometric precision for each filter is based solely on the positional uncertainty relative to the center of the coronagraph mask. The combined astrometry includes an additional term to account for uncertainty in the stellar position behind the mask (7 mas in each direction).

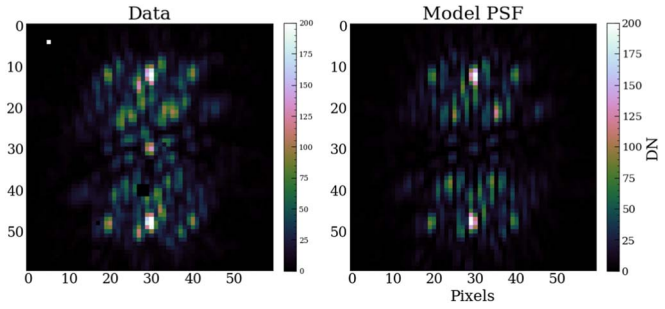

Figure 7. Left: an example of the raw MASKLWB coronagraph data for an image in the F360M filter. Right: the best-fit model PSF simulated using the most recent preceding OPD map, used to measure the centroid of the star.

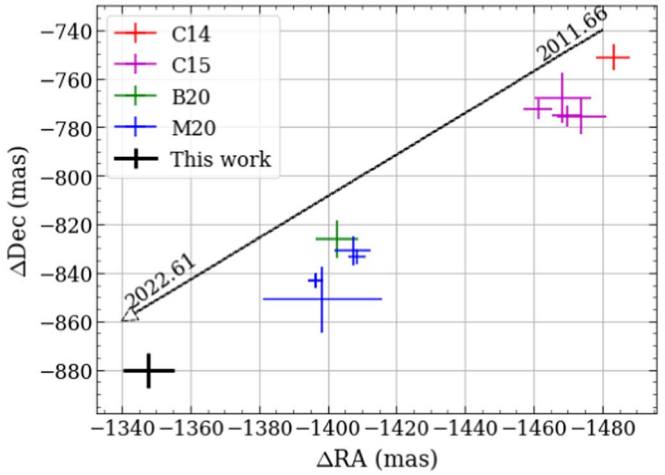

Figure 8. Astrometric position of HD 19467 B relative to its parent star, compared with previous measurements.

speckle structure. This suggests that bright companions could be observed without reference stars, significantly reducing the time spent on the observation. Future work will investigate the difference between reducing data with and without reference star observations. Future observations with a better defined position for the LWB coronagraph should also provide better contrast close in.

5. Orbit of HD 19467 B

Previous studies estimate the mass of HD 19467 B from 51 to 86 M_J through both model-based estimates and orbital analyses (Crepp et al. 2014; Maire et al. 2020; Brandt et al. 2021a). We analyze new RVs and provide an updated dynamical mass estimate including our new relative astrometry and additional RV measurements.

First, we fit the new and previously measured RVs from HIRES and HARPS (Trifonov et al. 2020) using the `RadVel`[21] software (Fulton et al. 2018). With the addition of the new data, we measure a linear slope term of $\dot{\gamma} = -0.00412 \pm 0.00027$ m s^{-1} d^{-1} with strong significance. We attempt to fit for curvature and tentatively detect a curvature term of $\ddot{\gamma} = 1.7^{+0.81}_{-0.78} \times 10^{-7}$ m s^{-1} d^{-2} at 2.1σ. Model comparison using ΔBIC and the corrected Akaike information criterion, AIC$_c$ (ΔAIC$_c$; Burnham & Anderson 2002) show nearly indistinguishable model fits to trend-only and trend-plus-curvature models. A detection of curvature can place strong constraints on the companion orbit, especially for higher-eccentricity systems. Figure 11 shows the RV data plotted over the maximum likelihood model. Appendix 2.2 contains a more detailed description of the fit comparison and the new RVs used in the analysis.

For the full orbital analysis we include all available RV measurements from HARPS (Trifonov et al. 2020) and HIRES (HIRES data including the new measurements tabulated in Appendix B), relative astrometry (Crepp et al. 2014, 2015; Bowler et al. 2020; Maire et al. 2020; listed in Table 6), and absolute astrometry from Hipparcos and Gaia as described in Brandt et al. (2021a), which takes advantage of the proper motion anomalies between Hipparcos and Gaia EDR3 and the Hipparcos–Gaia long-term trend. We utilize the cross-calibrated catalog of Hipparcos–Gaia accelerations presented in Brandt (2021).

We use `orvara` (Brandt et al. 2021b) to fit orbits to the RVs, absolute astrometry, and relative astrometry. `orvara` is an orbit-fitting code that uses `ptemcee`, a parallel-tempered MCMC scheme (Foreman-Mackey et al. 2013; Vousden et al. 2016). Following the orbital analysis in Brandt et al. (2021a), we apply a geometric prior to inclination and log-flat priors to the semimajor axis and companion mass. We apply uniform priors to the remaining orbital elements. Log-flat priors are applied to the RV jitters. We adopt a mass of $M_* = 0.96 \pm 0.02\,M_\odot$ based on the analysis in Section 3 using asteroseismology, spectroscopy, and Gaia data.

We first predict the position of HD 19467 B in the current epoch leaving out the new relative astrometry measured with NIRCam, but including all other data. Figure 12 shows that our measurement is consistent with the prediction of the best-fit orbits using previous measurements.

[21] https://radvel.readthedocs.io/en/latest/

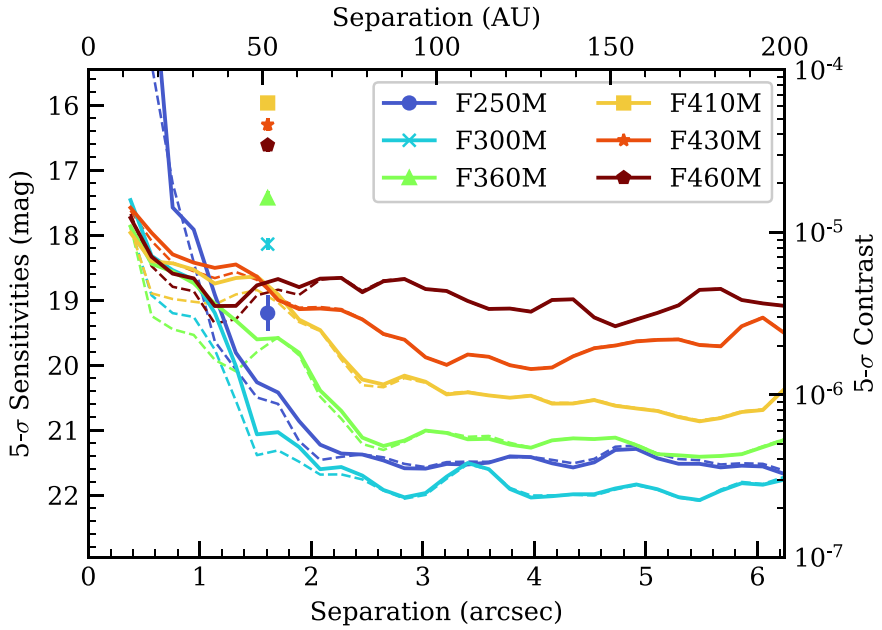

Figure 9. Contrast curves for all filters. The solid lines indicate ADI, and the dashed lines indicate ADI and RDI using synthetic PSFs. DThe data points indicate the HD 19467 B detections. The use of synthetic PSFs provides the diversity necessary to obtain enhanced contrast at small angular separations.

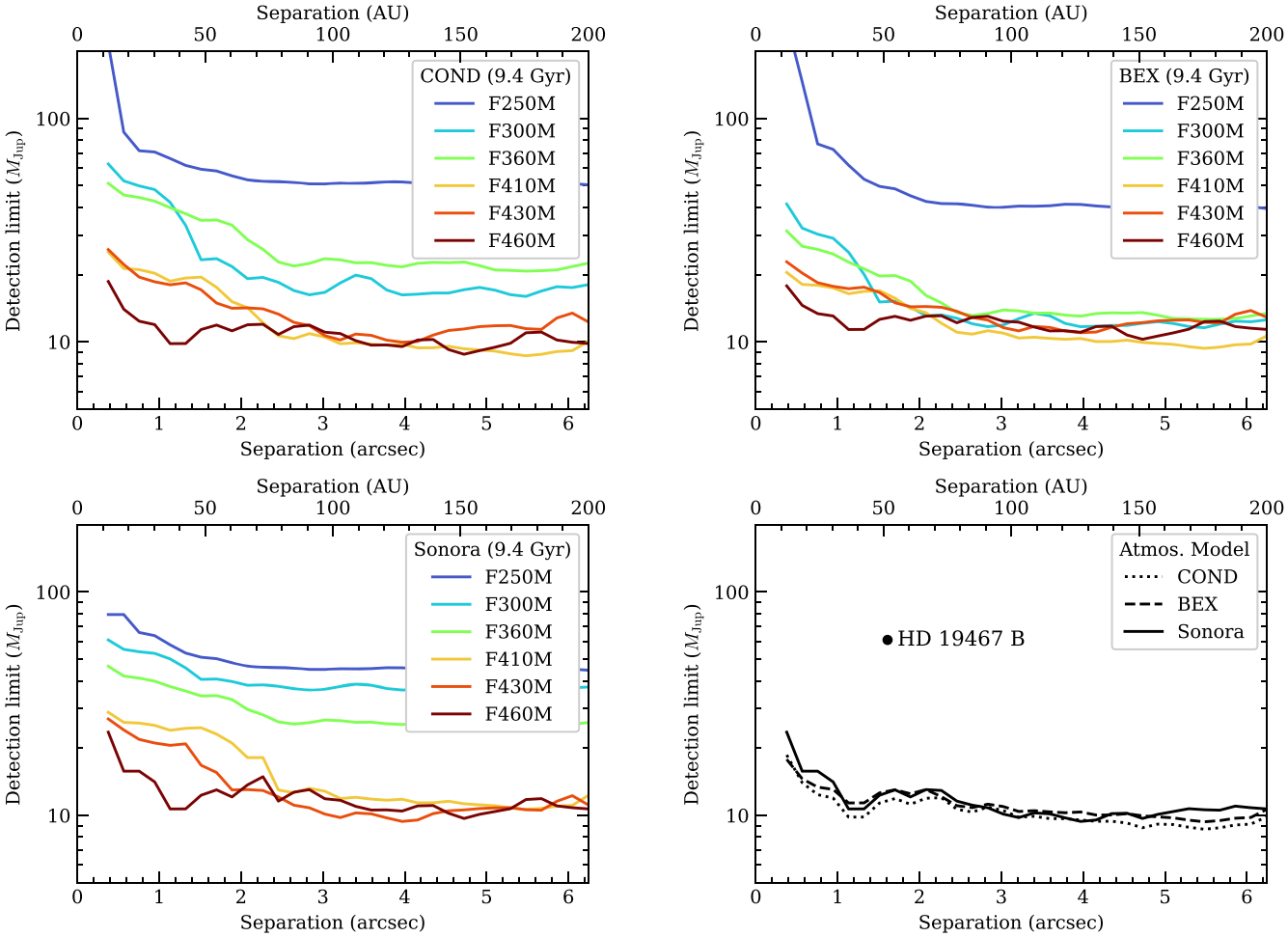

Figure 10. Detection limits (5σ) for each filter, in terms of companion mass. The first three panels show the limits for three different atmospheric evolution models (COND, Bex, and Sonora), while the last panel compares the overall detection limit for each of the models. A mass estimate from atmospheric model fitting (Section 6) is shown as a point in the lower right figure (61 M_J at $1\farcs61$).

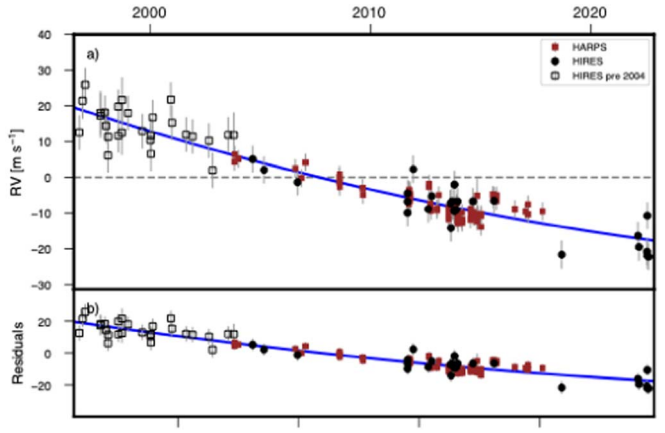

Figure 11. Best-fit single-companion Keplerian orbital model for HD 19467 to RVs measured for HD 19467 by HIRES by the California Legacy Survey (Rosenthal et al. 2021), new HIRES observations, and HARPS (Trifonov et al. 2020). The fit slightly favors a curvature term.

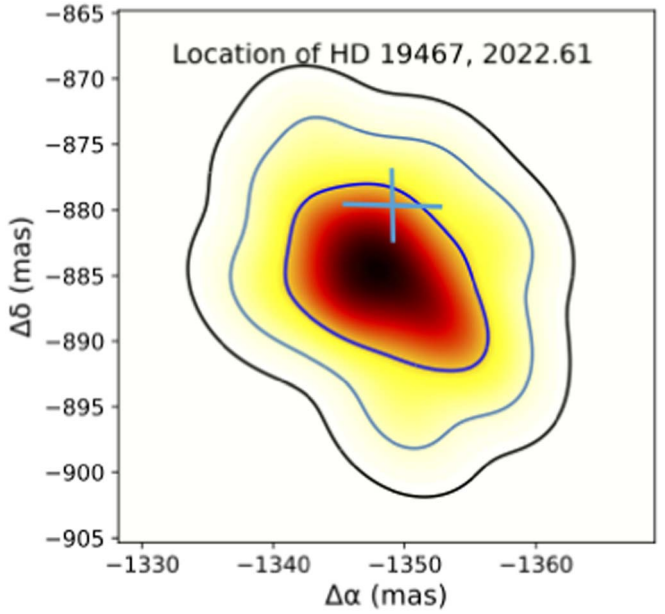

Figure 12. Orvara prediction of relative astrometry at the 2022 August 12 epoch. The measured astrometry is consistent with the prediction.

Table 6
Imaging Astrometry

epoch−2,450,000	Filter	ρ (mas)	$\rho_{\rm err}$	PA (deg)	PA$_{\rm err}$
Astrometry from Crepp et al. (2014)					
5804.1	K'	1662.7	4.9	243.14	0.19
5933.8	H	1665.7	7.0	242.25	0.26
5933.8	K'	1657.3	7.2	242.39	0.38
6166.1	K'	1661.8	4.4	242.19	0.15
6205.0	Ks	1653.1	4.1	242.13	0.14
Astrometry from Maire et al. (2020)					
8032.3	L'	1637	19	238.68	0.47
8061.2	K1	1636.7	1.8	239.39	0.13
8061.2	K2	1634.4	5.0	239.44	0.21
8409.3	H2	1631.4	1.6	238.88	0.12
8409.3	H3	1631.4	1.6	238.88	0.12
New Astrometry (this work; see Table 5)					
9803.9	2.5–4.6 μm	1607.6	7	236.84	0.25

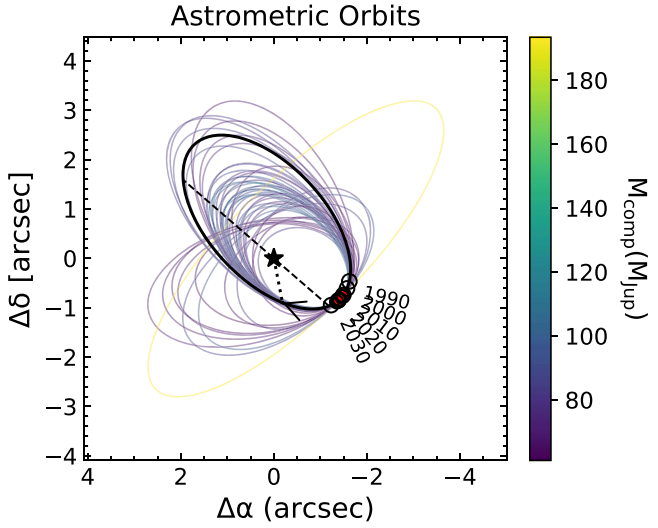

Figure 13. A selection of orbits from the MCMC posteriors.

Table 7
Orbit Fit Results

Parameter	Units	Value
Jitter	m/s	$3.17^{+0.25}_{-0.23}$
M_{pri}	M_*	$0.961^{+0.022}_{-0.022}$
M_{sec}	$M_{\rm J}$	81^{+14}_{-12}
Semimajor axis	au	53^{+19}_{-10}
$\sqrt{e}\sin\omega$		$-0.586^{+0.068}_{-0.061}$
$\sqrt{e}\cos\omega$		$0.08^{+0.29}_{-0.32}$
Inclination	deg	$127.9^{+8.1}_{-5.7}$
Ascending node	deg	$48.9^{+240}_{-7.3}$
Mean longitude	deg	$192.7^{+7.7}_{-123}$
Parallax	mas	$31.226^{+0.037}_{-0.037}$
Period	year	382^{+220}_{-108}
Argument of periastron	deg	278^{+27}_{-29}
Eccentricity		$0.416^{+0.092}_{-0.070}$
Semimajor axis	mas	1664^{+598}_{-328}
T_0	JD	2486667^{+51547}_{-4207}
Mass ratio		$0.080^{+0.014}_{-0.012}$

Next, we fit for the orbital parameters including our new relative astrometry measurement from NIRCam. Table 7 summarizes the orbit fit results. We infer a mass of $81^{+14}_{-12}\,M_{\rm J}$. Our mass estimate for HD 19467 B is within 1σ of the prior estimates from in Brandt et al. (2021a; $65.4^{+5.9}_{-4.6}\,M_{\rm J}$) and Maire et al. (2020; $74^{+12}_{-9}\,M_{\rm J}$). We infer an eccentricity of $0.416^{+0.092}_{-0.07}$, which is consistent with recent measurements in Brandt et al. (2021a), 0.54 ± 0.11, Maire et al. (2020), 0.56 ± 0.09, and Bowler et al. (2020), $0.39^{+0.26}_{-0.18}$. We infer a period of 386^{+220}_{-108} yr, which is consistent with prior orbital analyses (Bowler et al. 2020; Maire et al. 2020; Brandt et al. 2021a). The tentative evidence for curvature from the new RVs may indicate that the orbit is close to periastron passage. Given the high eccentricity, it could be a critical time to monitor this system.

Figure 13 shows a selection of orbits from MCMC posteriors overlaid with the relative astrometry used in the fit, and Figure 14 displays a corner plot of the MCMC posteriors for the orbital parameters.

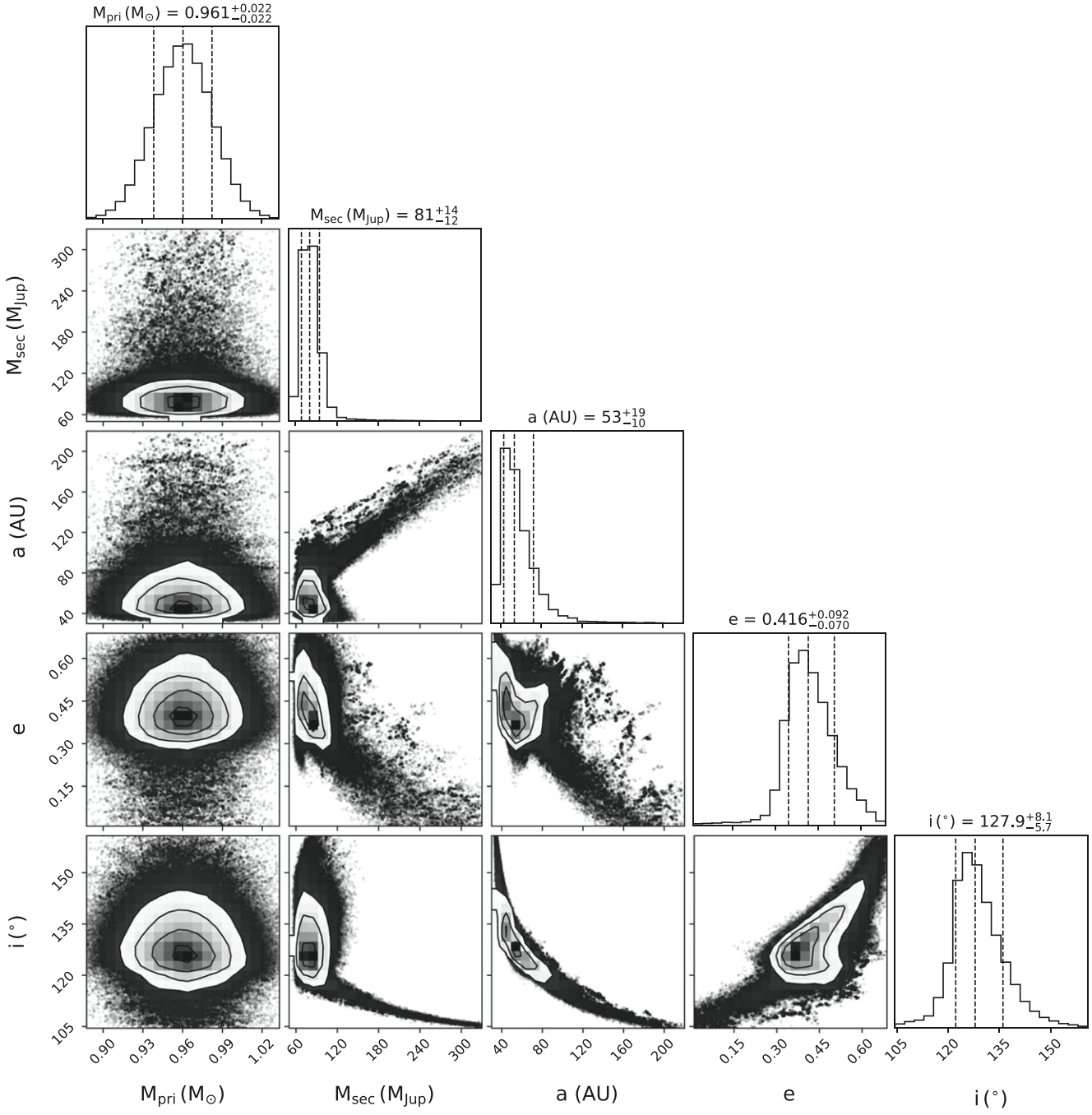

Figure 14. Corner plot showing the MCMC posteriors for selected orbital parameters.

6. Atmosphere and Evolution Model Comparison

In the following sections we show a preliminary comparison of our near-IR photometry from NIRCam with brown dwarf atmospheric models, focusing on the Sonora models (Karalidi et al. 2021; Marley et al. 2021). In our spectral fitting, we only use a spectral model grid with a solar carbon-to-oxygen ratio.

The Sonora-Bobcat cloudless atmospheric models assume that the atmospheric composition is in thermochemical equilibrium and solve radiative transfer equations for a self-consistent temperature–pressure profile. The model grid covers temperatures from 200 to 2400 K, gravities from 10 to 3160 $\mathrm{m\,s^{-2}}$, and metallicities from $[\mathrm{Fe/H}] = -0.5$ to 0.5. The model spectra have a spectral resolution ranging from 0.6 to 20 μm.

The Sonora-Cholla cloudless models assume chemical disequilibrium. These models assume that the atmospheres have solar metallicity (Lodders 2010) with cloud-free atmospheric structures. The models are computed using the `Picaso v3.0` atmospheric model (Mukherjee et al. 2022). By including an eddy diffusion parameter, K_{zz}, that ranges from 10^2 to $10^7\,\mathrm{cm^2\,s^{-1}}$ as an input parameter, the Cholla models simulate the dynamical mixing that drives various molecular species like CH_4, CO, H_2O, and NH_3 out of their thermochemical equilibrium abundances. The Cholla models span over a temperature grid of 500–1300 K and a gravity grid of 56 to 3160 $\mathrm{m\,s^{-2}}$.

First, we perform a basic χ^2 comparison of new JWST photometry to the Sonora models (Karalidi et al. 2021; Marley

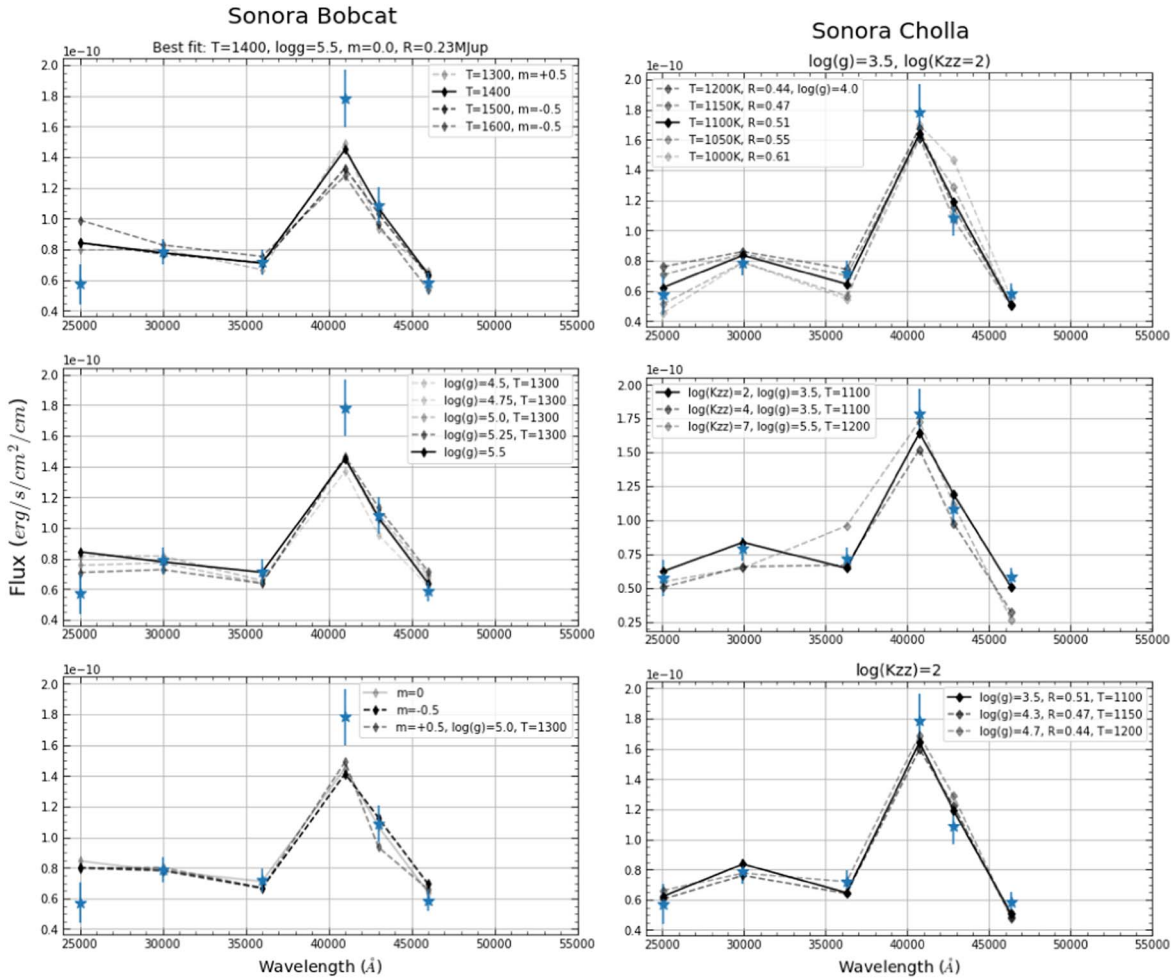

Figure 15. Left: measured photometry from NIRCam plotted alongside a few closely matching scenarios from the Sonora-Bobcat models, letting the radius vary. Right: measured photometry from NIRCam plotted alongside a few closely matching scenarios from the Sonora-Cholla models, which include chemical disequilibrium parameterized by the eddy diffusion parameter, log (K_{zz}).

et al. 2021). We also perform an MCMC fit of the model grids with both our new photometry and previously published medium-resolution spectrum obtained with SPHERE-IRDIS-LSS (Mesa et al. 2020) and ground-based photometry from SPHERE-IRDIS (Maire et al. 2020). From this we derive a bolometric luminosity and determine a model-dependent mass estimate.

6.1. Model Comparison with NIRCam Photometry Only

We compare the NIRCam photometry with both the Sonora-Bobcat and Sonora-Cholla model grids to highlight the broad features of the 2–5 μm flux. We allow the radius scaling to vary when fitting the models to our NIRCam photometry, which is generally consistent with radii much smaller than, e.g., those predicted by the Sonora-Bobcat grid evolutionary tables.

We find that the Bobcat models do not simultaneously capture both the local flux peak at 3 μm and the steep drop in flux from 4 to 5 μm. In general the Bobcat grid favors higher gravity and lower or zero metallicity. However, none of the fits capture all of the photometry perfectly. A model spectrum at an effective temperature of $T_{\rm eff} = 1400$ K best matches the data, but does not fully capture the peak flux at $\sim$4 μm with the drop off at longer wavelengths. The gravity and metallicity do not have a strong effect on the fit.

The Sonora-Cholla models, which include effects of disequilibrium chemistry, provide better fits to the photometry, but suggest a low value for the gravity as well as a small radius to scale the flux. The best-fit model has $T_{\rm eff} = 1200$ K, $g = 31$, and $log(K_{zz}) = 2$. Figure 15 (right) shows the best-fitting Cholla model, with a few model grid points that vary in temperature, eddy diffusion parameter, and gravity. We note that while lower gravity is favored, the gravity does not strongly affect the shape of the photometry-only profile, as can be seen in the third panel. Near-IR spectroscopy with JWST will be able to distinguish the features of gravity further.

Overall, the best-fit Sonora-Cholla model provides a better fit than the best-fit Sonora-Bobcat model. As can be seen in Figure 15, the Cholla models are better able to capture the lower flux at shorter wavelengths simultaneously, the peak at $\sim$4 μm, and the subsequent drop in flux, favoring a lower temperature that is more consistent with previous estimates. This suggests that modeling disequilibrium chemistry may be necessary for understanding the atmosphere and evolution of HD 19467 B.

6.2. Model Fit to the 1–5 μm Data

We fit the Sonora-Cholla cloudless models to a composite data set that consists of JWST photometry, IRDIS spectra

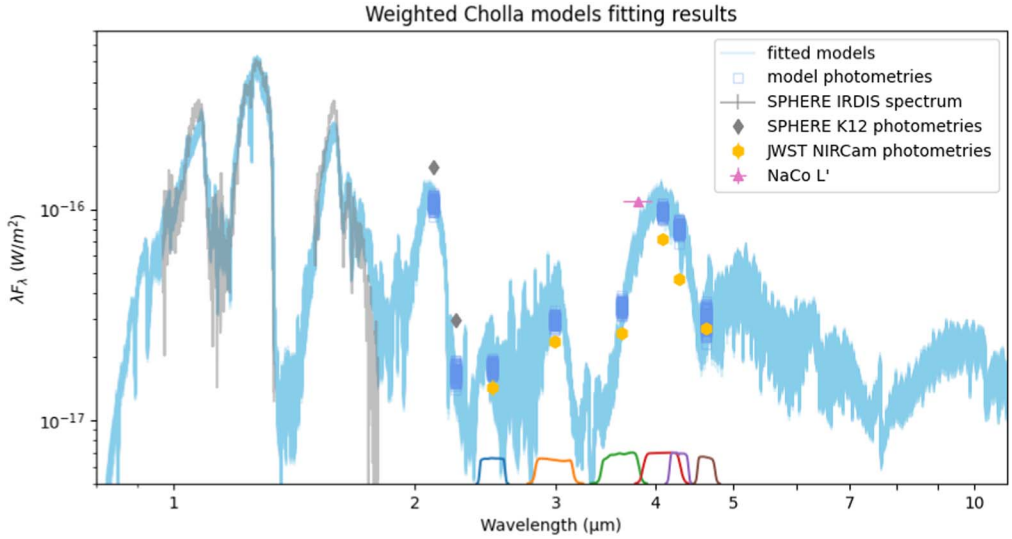

Figure 16. The comparison of the fitted Cholla model spectra (light blue lines) to the SPHERE/IRDIS-LSS 1–1.8 μm spectra (gray lines), SPHERE/IRDIS-K12 photometry (gray diamonds), NACO *L'* band (pink triangle), and JWST NIRCam photometry (golden hexagon) shows that it is challenging for the models to explain the near-IR and mid-IR spectra and photometry simultaneously. The semitransparent light blues lines are the 1000 Cholla cloudless model spectra sampled from the posterior distribution of MCMC fitting results. The blue squares are the effective photometry from the model spectra samples in the corresponding NIRCam filters. The transmission curves of the JWST NIRCam broadband filters are plotted in colored lines at the bottom of the plot. The *y*-axis is in units of intensity (W m^{-2}).

(Mesa et al. 2020), and SPHERE *K*12 band photometry (Maire et al. 2020) to constrain the temperature and gravity of HD 19487 B. For the IRDIS spectra, we exclude spectral points with negative flux values. We include an additional uncertainty of 7%, similar to the *J*- and *H*-band absolute flux uncertainties of HD 19467 (Table 3 of Mesa et al. 2020), to account for the possible offset in the absolute flux levels.

We linearly interpolate the Cholla model spectral grid to a finer grid with smaller step sizes in the temperature, gravity, and eddy diffusion parameter. In addition to these three parameters, the other free parameter in the spectral fitting is the scaling factor, which is the square of the ratio of brown dwarf radius to the distance (32.03 pc). We use `pyphot`[22] to calculate the broadband photometry of the model spectra.

Our model fitting algorithm minimizes a cost function that sums the squared difference between the model spectra and data, weighted by the observational uncertainties, σ, and the intensities, w, as shown in the following:

$$\text{cost function} = \sum_{i=1}^{N} \left\{ w_i \frac{F_{\lambda,i}(\text{model}) - F_{\lambda,i}(\text{data})}{\sigma_i} \right\}^2, \text{ where,}$$
$$w_i = \frac{F_{\lambda,i}\Delta\lambda_i}{\max(F_{\lambda,i}\Delta\lambda_i)}, \quad (1)$$

where $\Delta\lambda_i$ is the wavelength coverage of a data point and the intensity weighting is normalized by the highest intensity among the data points. We include the intensity weighting in the cost function so that a photometric point with high intensity carries more weight in the fitting process than a spectral point with low intensity even though both could have a similar S/N, since the photometric points contain a larger fraction of the total flux measured. We then use `emcee` (Foreman-Mackey et al. 2017) to sample the posterior distribution of the fitted parameters with the MCMC method. We adopt uniform priors of the temperature, logarithmic gravity, and eddy diffusion parameter. We run the MCMC chain with 200 walkers for 20,000 steps. Based on the posterior distribution of the MCMC chains, we derive a best-fit temperature of 1080 ± 22 K, gravity of $\log(g) = 4.60^{+0.2}_{-0.1}$, eddy diffusion parameter of $\log K_{zz} = 3.1^{+0.6}_{-0.4}$, and radius R of $0.62 \pm 0.03\,R_J$. The value for the radius is lower than the expected radius at 9 Gyr, $\sim 0.8\,R_{Jup}$, according to the evolutionary model grid at similar parameters. Prior modeling work has noted a common discrepancy between the expected radius from evolutionary models and the radius required to match the flux of a given temperature that best fits the atmospheric model (e.g., Barman et al. 2011; Marley et al. 2012; Lavie et al. 2017). Maire et al. (2020) explored radius agreement with evolutionary tracks with different model atmospheres that included various levels of clouds in the atmospheres. Future observations, especially spectroscopy will further help constrain atmospheric models.

We draw 100 parameter sets from the posterior distribution and plot the corresponding model spectra in Figure 16. Figure 16 suggests that the model spectra provide a qualitatively good match to the data but there are some significant residuals, especially in the *K*-band photometry. We remain cautious about the inferred parameters and the seemingly small uncertainties given the imperfect fit between the data and model spectra. However, while the absolute flux calibrations may account for some of the discrepancy between the data sources, the discrepancy alone is not enough to account for inconsistencies between the best-fit atmospheric model and evolutionary grid predictions. Clouds, which likely drive the rotational modulation of many T dwarfs (e.g Manjavacas et al. 2019) and are not included in the Cholla models, could play a key role in shaping the HD 19467 B emission spectra. Future simultaneous observation in the near-IR and mid-IR regions will be useful for testing the role of clouds in the atmosphere of HD 19467 B with well-constrained age and host-star metallicity.

[22] https://github.com/mfouesneau/pyphot

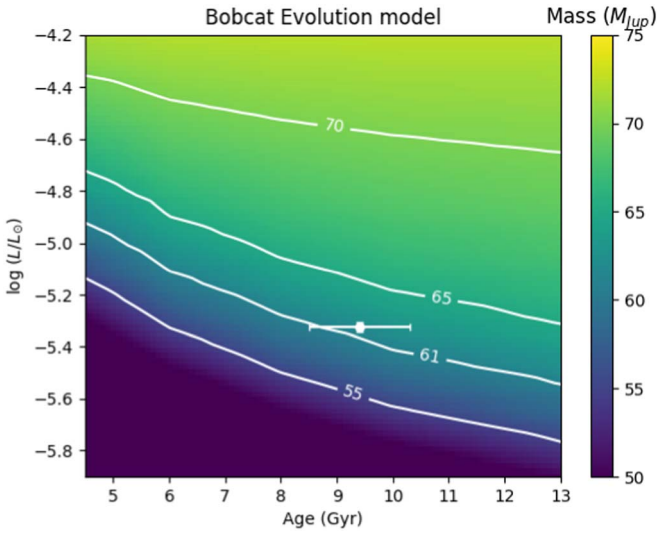

Figure 17. Based on the bolometric luminosity and age, the Bobcat evolution models suggest that HD 19467 B has a mass of $62 \pm 1\,M_J$. The colors indicate the masses predicted by Bobcat evolution models. The white contour lines show the bolometric luminosity and age with a fixed mass. The uncertainty of HD 19467 B's bolometric luminosity is around 4%.

6.3. Bolometric Luminosity

The 2–5 μm JWST NIRCam broadband photometry, in combination with the ground-based near-IR spectra and photometry, are crucial for pinning down the bolometric luminosity of a ~1000 K object. We integrate the flux density over the observed data including the previously published IRDIS-LSS spectra (0.97–1.335 μm and 1.50–1.80 μm) , ground-based K-band photometry (2.059–2.161 μm and 2.1965–2.3055 μm), and the six JWST NIRCam broadband photometry. The flux integral in the observed wavelength regions is $(3.28 \pm 0.2) \times 10^{-6}\,L_\odot$.

We utilize the fitted model spectra in Section 6 to extrapolate flux density beyond the observed wavelength region and estimate the bolometric luminosity. We find that the observational data account for around 72% of the bolometric luminosity. The estimated total bolometric luminosity is $(4.75 \pm 0.2) \times 10^{-6}\,L_\odot$, or $\log(L/L_\odot) = -5.32 \pm 0.02$. Based on the combination of JWST NIRCam high-precision photometry and ground-based data, our results suggest that we can accurately derive the bolometric luminosity at a 4% precision level.

Based on the independently estimated age and bolometric luminosity, we then use the Bobcat evolution model to estimate the mass of HD 19467 B. After linearly interpolating the mass as a function of age and bolometric luminosity, we derive that the mass is $62 \pm 1\,M_J$. Figure 17 shows the Sonora-Bobcat evolution model and where our bolometric luminosity estimate lies. By comparing the mass derived from the age and L_{bol} to the dynamical mass, ($81^{+14}_{-12} M_J$), we conclude that the two masses are consistent with each other within about 2σ.

The NIRSpec IFU observations planned for later this year (PID #1414) will provide a much more complete characterization of the atmosphere of HD 19467 B, helping to pin down parameters such as metallicity and $T_{\rm eff}$.

7. Conclusions

We have demonstrated the performance of the JWST NIRCam LWB coronagraph on the known binary system HD 19467 B. Despite missing reference star observations, we are able to recover the companion with high significance in all six medium NIRCam bands used for the observations.

The main results of this study are as follows:

1. The MASKLWB coronagraph works well for separations below 1″ (for medium filters excluding F250M) at contrasts of 10^{-5} and better, even without a reference star when angular diversity is utilized. This is expected to improve in the near future when coronagraphic mask locations are refined through instrument calibration observations.
2. Given the superb stability of JWST, and regular OPD measurements available, we are able to incorporate synthetic reference images to subtract speckles further, following ADI subtraction, and improve the S/N of the detections. Future observations with reference observations can be compared with the results presented in this study.
3. We estimate the age of the HD19467 system by combining spectroscopy and Gaia astrometry with asteroseismic constraints from TESS, finding an age of 9.4 ± 1.0 Gyr, supporting older estimates of the age. We provide updated parameters for the host star HD19467.
4. We estimate a dynamical mass of HD 19467 B of $81^{+14}_{-12} M_J$, contributing new relative astrometry from NIRCam and RVs from HIRES, and detect tentative evidence of curvature in the orbit fit to the RVs.
5. A comparison of atmospheric and evolutionary models to our new 2–5 μm photometry favors models that include disequilibrium chemistry.
6. A global fit to the photometry and spectroscopy from this study and ground-based observations show some tension between the instrument-to-instrument relative fluxes and the models.
7. The model-derived mass of $62 \pm 1\,M_J$ is lower than the dynamical mass estimate, but within 2σ.

The NIRCam observations provide the highest fidelity 3–5 μm photometry to date of HD 19467 B, and give an early test of atmospheric and evolutionary models that JWST will continue to test throughout the mission. Future observations with NIRSpec (PID #1414) will further elucidate discrepancies in model spectra and help characterize the chemistry of HD 19467 B. Improvements in the near future through instrument calibration observations will further refine the performance of the coronagraphic mask placement and the performance of the MASKLWB mode.

The authors acknowledge useful discussions with G. Mirek Brandt and Eric Nielsen. We also thank Dino Mesa for providing the data for the near-IR spectrum of HD 19467 B. We thank the anonymous reviewer for providing useful suggestions for improving the clarity of this work.

The authors acknowledge this work was authored by employees of Caltech/IPAC under contract 80GSFC22CA003 with the the National Aeronautics and Space Administration. Some of the research described in this publication was carried out at the Jet Propulsion Laboratory, California Institute of Technology, under a contract with the National Aeronautics and Space Administration (80NM0018D0004). T.L.R acknowledges support from the NASA Science Mission Directorate under WBS 411672.05.05.02.01. D.J. is supported

by NRC Canada and by an NSERC Discovery Grant. L.E.U. C.'s research was supported by an appointment to the NASA Postdoctoral Program at the NASA Ames Research Center, administered by Oak Ridge Associated Universities under contract with NASA. D.R.H. and D.H. acknowledge support from the Research Corporation for Science Advancement (Scialog award #26996) and the National Science Foundation (AST-2009828). D.H. also acknowledges support from the Alfred P. Sloan Foundation and the National Aeronautics and Space Administration (80NSSC21K0652,80NSSC22K0303).

Some of the data presented in this paper were obtained from the Mikulski Archive for Space Telescopes (MAST) at the Space Telescope Science Institute. The specific observations analyzed can be accessed via 10.17909/v8m9-xk98 (JWST) and 10.17909/t9-st5g-3177 (TESS).

This research has made use of the SIMBAD database, operated at CDS, Strasbourg, France.

Some of the data presented herein were obtained at the W. M. Keck Observatory, which is operated as a scientific partnership among the California Institute of Technology, the University of California and the National Aeronautics and Space Administration. The Observatory was made possible by the generous financial support of the W. M. Keck Foundation. The authors wish to recognize and acknowledge the very significant cultural role and reverence that the summit of Maunakea has always had within the indigenous Hawaiian community. We are most fortunate to have the opportunity to conduct observations from this mountain.

Software: SciPy (Virtanen et al. 2020), NumPy (Harris et al. 2020), Matplotlib (Hunter 2007), WebbPSF (Oschmann et al. 2014), PyKLIP (Wang et al. 2015), synphot (Lim & Hanley 2016), pysynphot (STScI Development Team 2013), pyphot (Fouesneau 2022).

Appendix A
KLIP Forward Model of the Data

We compute a forward model of the PSF-subtracted image according to Pueyo (2016) to account for over- and self-subtraction effects. ADI imaging is particularly susceptible to self-subtraction effects, especially when there is little angular diversity, such as our data, which contain only two roll angles separated at $\sim 8^{\circ}$. Modeling these effects is essential for appropriately estimating the properties of the signal (flux and position). Figure 18 displays a comparison between the forward model and the PSF-subtracted image corresponding to the images displayed in Figure 3.

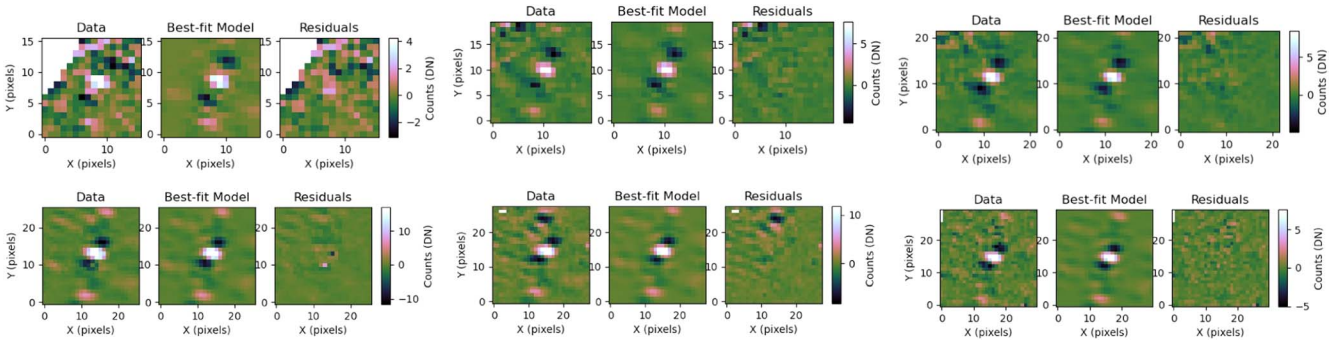

Figure 18. The KLIP forward model that accounts for over-subtraction effects compared to the PSF-subtracted data in each filter: F250M, F300M, F360M, F410M, F430M, and F460M.

Appendix B
Keplerian Orbit Fit to HD 19467 RVs

We fit a Keplerian orbit model to the RVs of HD 19467 from HIRES and HARPS instruments, the latter published in Trifonov et al.2020, catalog JA + A636A74rvbank table entries DRVmlcnzp and e_DRVmlcnzp. HIRES RVs, along with the new measurements are presented in Table 8. Using `RadVel` (Fulton et al. 2018), we determine that a model with a curvature term is slightly favored over a model without curvature, however the trend-only and trend-plus-curvature models are nearly indistinguishable (Table 9), based on ΔBIC and ΔAIC metrics. This is the first tentative evidence of curvature measured for HD 19467. Future follow-up is needed to support this finding further.

Table 8
HIRES RV Observations

Instrument	BJD_{TDB}	RV	RV Error
HIRES	2450366.019	20.64	1.47
HIRES	2450418.943	29.50	2.17
HIRES	2450461.84	34.01	1.30
HIRES	2450715.103	26.13	4.20
HIRES	2450716.111	25.36	4.31
HIRES	2450786.847	23.29	2.38
HIRES	2450786.86	27.42	1.51
HIRES	2450806.904	22.50	1.50
HIRES	2450837.744	14.19	1.41
HIRES	2450839.743	19.41	1.49
HIRES	2451012.119	27.88	1.40
HIRES	2451013.12	19.74	1.31
HIRES	2451070.116	20.60	4.26
HIRES	2451072.984	29.72	4.36
HIRES	2451171.777	26.06	1.48
HIRES	2451410.128	21.00	1.51
HIRES	2451543.847	18.48	1.60
HIRES	2451551.792	19.77	1.47
HIRES	2451552.844	14.65	1.73
HIRES	2451582.73	24.84	1.70
HIRES	2451882.806	29.84	1.62
HIRES	2451900.783	23.36	1.48
HIRES	2452134.08	20.03	1.58
HIRES	2452242.908	19.50	1.42
HIRES	2452516.022	18.34	1.62
HIRES	2452575.902	10.04	1.72
HIRES	2452835.128	19.96	1.84
HIRES	2452926.089	19.92	4.43
HIRES	2453240.043	11.43	1.16
HIRES	2453427.785	8.38	1.20
HIRES	2453984.039	5.01	1.08
HIRES	2455807.035	−3.65	1.23
HIRES	2455808.105	−0.48	1.42
HIRES	2455809.088	1.84	1.22
HIRES	2455903.779	8.54	1.33
HIRES	2456152.11	−2.44	1.18
HIRES	2456210.015	1.14	1.49
HIRES	2456519.085	−0.97	1.28
HIRES	2456530.025	−7.90	1.20
HIRES	2456548.035	−0.47	1.33
HIRES	2456586.036	−2.87	1.41
HIRES	2456587.965	−3.16	1.42
HIRES	2456588.997	4.29	1.41
HIRES	2456613.908	−2.82	1.38
HIRES	2456637.791	−0.19	1.45
	New data		
HIRES	2457245.143	−0.38	1.18
HIRES	2458367.035	−15.44	1.76
HIRES	2459632.706	−10.11	1.51
HIRES	2459649.719	−13.26	1.48
HIRES	2459780.128	−14.46	1.29
HIRES	2459786.103	−4.38	1.16
HIRES	2459787.129	−15.52	1.20

Table 9
Model Comparison

AICc Qualitative Comparison	Free Parameters	$N_{\rm free}$	$N_{\rm data}$	rms	$\ln \mathcal{L}$	BIC	AICc	ΔAICc
AICc-favored Model	$\dot{\gamma}$, $\ddot{\gamma}$, σ, γ	8	128	3.40	−330.13	695.02	673.41	0.00
Nearly indistinguishable	$\dot{\gamma}$, σ, γ	7	128	3.40	−332.43	692.91	673.88	0.47
Ruled out	σ, γ	6	128	9.50	−426.33	872.85	856.43	183.02

Appendix C
The MCMC Posterior Distribution for Spectral Fitting

Figure 19 shows the MCMC posterior distribution of the spectral fitting. The spatial structure seen in the posterior distribution reflects the step size of the temperature (10 K), gravity (0.025 dex), and $\log(K_{zz})$ (0.167) in the interpolated model grid. The sharp boundaries of radius at 0.5 $R_{\rm Jup}$ is reflects the lowest limit of radius range (0.5–1.5 $R_{\rm Jup}$) in the model fitting.

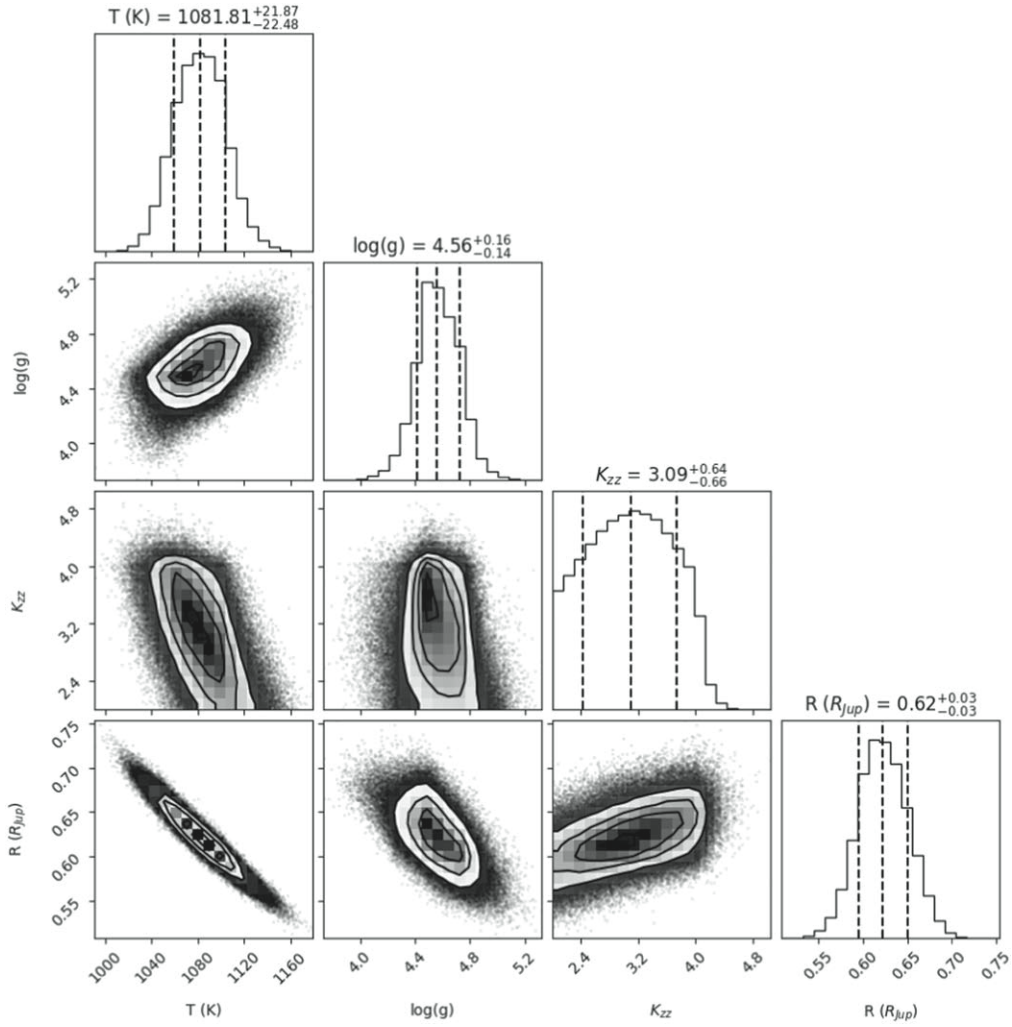

Figure 19. The posterior distribution of the MCMC fitting of Cholla models to the SPHERE-IRDIS spectra, SPHERE K12 photometry, and the JWST NIRCam photometry.

ORCID iDs

Alexandra Z. Greenbaum https://orcid.org/0000-0002-7162-8036
Jorge Llop-Sayson https://orcid.org/0000-0002-3414-784X
Ben W.P. Lew https://orcid.org/0000-0003-1487-6452
Geoffrey Bryden https://orcid.org/0000-0001-5966-837X
Marie Ygouf https://orcid.org/0000-0001-7591-2731
B. J. Fulton https://orcid.org/0000-0003-3504-5316
Daniel R. Hey https://orcid.org/0000-0003-3244-5357
Daniel Huber https://orcid.org/0000-0001-8832-4488
Sagnick Mukherjee https://orcid.org/0000-0003-1622-1302
Michael Meyer https://orcid.org/0000-0003-1227-3084
Jarron Leisenring https://orcid.org/0000-0002-0834-6140
Marcia Rieke https://orcid.org/0000-0002-7893-6170
Martha Boyer https://orcid.org/0000-0003-4850-9589
Laurie E. U. Chu https://orcid.org/0000-0002-1437-4463
Matthew De Furio https://orcid.org/0000-0003-1863-4960
Doug Johnstone https://orcid.org/0000-0002-6773-459X
Charles Beichman https://orcid.org/0000-0002-5627-5471

References

Aguirre Børsen-Koch, V., Rørsted, J. L., Justesen, A. B., et al. 2022, MNRAS, 509, 4344
Amara, A., & Quanz, S. P. 2012, MNRAS, 427, 948
Baraffe, I., Chabrier, G., Barman, T. S., Allard, F., & Hauschildt, P. H. 2003, A&A, 402, 701
Barman, T. S., Macintosh, B., Konopacky, Q. M., & Marois, C. 2011, ApJ, 733, 65
Bedding, T. R. 2014, in Canary Islands Winter School of Astrophysics, Vol. XXII, ed. P. L. Pallé & C. Esteban (Cambridge: Cambridge Univ. Press), 60
Beichman, C. A., Krist, J., Trauger, J. T., et al. 2010, PASP, 122, 162
Bohlin, R. C., Meszaros, S., Fleming, S. W., et al. 2017, AJ, 153, 234
Bowler, B. P., Blunt, S. C., & Nielsen, E. L. 2020, AJ, 159, 63
Brandt, G. M., Dupuy, T. J., Li, Y., et al. 2021a, AJ, 162, 301
Brandt, T. D. 2021, ApJS, 254, 42
Brandt, T. D., Dupuy, T. J., Li, Y., et al. 2021b, AJ, 162, 186
Brewer, J. M., Fischer, D. A., Valenti, J. A., & Piskunov, N. 2016, ApJS, 225, 32
Brown, T. M., Gilliland, R. L., Noyes, R. W., & Ramsey, L. W. 1991, ApJ, 368, 599
2002, in Model Selection and Multimodel Inference: A Practical Information-Theoretic Approach, Burnham, K. P., & Anderson, D. R. (ed.) (New York: Springer)
Butler, R. P., Marcy, G. W., Williams, E., et al. 1996, PASP, 108, 500
Butler, R. P., Vogt, S. S., Laughlin, G., et al. 2017, AJ, 153, 208
Carter, A. L., Hinkley, S., Kammerer, J., et al. 2022, arXiv:2208.14990
Casagrande, L., Lin, J., Rains, A. D., et al. 2021, MNRAS, 507, 2684
Choi, J., Dotter, A., Conroy, C., et al. 2016, ApJ, 823, 102
Chontos, A., Huber, D., Sayeed, M., & Yamsiri, P. 2021, JOSS, 7, 3331
Corsaro, E., McKeever, J. M., & Kuszlewicz, J. S. 2020, A&A, 640, A130
Crepp, J. R., Johnson, J. A., Howard, A. W., et al. 2014, ApJ, 781, 29
Crepp, J. R., Rice, E. L., Veicht, A., et al. 2015, ApJL, 798, L43
Cutri, R. M., et al. 2012, yCat, II/311
Cutri, R. M., Skrutskie, M. F., van Dyk, S., et al. 2003, yCat, II/246
Foreman-Mackey, D., Agol, E., Ambikasaran, S., & Angus, R. 2017, AJ, 154, 220
Foreman-Mackey, D., Hogg, D. W., Lang, D., & Goodman, J. 2013, PASP, 125, 306
Fouesneau, M. 2022, pyphot, 1.4.3.
Fulton, B. J., Petigura, E. A., Blunt, S., & Sinukoff, E. 2018, PASP, 130, 044504
García, R. A., & Ballot, J. 2019, LRSP, 16, 4
Girard, J. H., Leisenring, J., Kammerer, J., et al. 2022, Proc. SPIE, 12180, 121803Q
Gomes da Silva, J., Santos, N. C., Adibekyan, V., et al. 2021, A&A, 646, A77
Harris, C. R., Millman, K. J., van der Walt, S. J., et al. 2020, Natur, 585, 357
Huber, D., Stello, D., Bedding, T. R., et al. 2009, CoAst, 160, 74
Huber, D., Chaplin, W. J., Christensen-Dalsgaard, J., et al. 2013, ApJ, 767, 127
Huber, D., Zinn, J., Bojsen-Hansen, M., et al. 2017, ApJ, 844, 102
Huber, D., White, T. R., Metcalfe, T. S., et al. 2022, AJ, 163, 79
Hunter, J. D. 2007, CSE, 9, 90
Jakobsen, P., Ferruit, P., Alves de Oliveira, C., et al. 2022, A&A, 661, A80
Jenkins, J. M., Twicken, J. D., McCauliff, S., et al. 2016, Proc. SPIE, 9913, 99133E
Karalidi, T., Marley, M., Fortney, J. J., et al. 2021, ApJ, 923, 269
Krist, J. E., Burrows, C. J., Stapelfeldt, K. R., et al. 1997, ApJ, 481, 447
Krist, J. E., Beichman, C. A., Trauger, J. T., et al. 2007, Proc. SPIE, 6693, 66930H
Lafreniere, D., Marois, C., Doyon, R., Nadeau, D., & Artigau, E. 2007, ApJ, 660, 770
Lavie, B., Mendonça, J. M., Mordasini, C., et al. 2017, AJ, 154, 91
Lim, P. L., & Hanley, C. 2016, synphot, Zenodo, doi:10.5281/zenodo.3673988
Linder, E. F., Mordasini, C., Mollière, P., et al. 2019, A&A, 623, A85
Lodders, K. 2010, in Formation and Evolution of Exoplanets, ed. R. Barnes (New York: Wiley), 157
Lorenzo-Oliveira, D., Freitas, F. C., Meléndez, J., et al. 2018, A&A, 619, A73
Maire, A. L., Molaverdikhani, K., Desidera, S., et al. 2020, A&A, 639, A47
Manjavacas, E., Apai, D., Lew, B. W. P., et al. 2019, ApJL, 875, L15
Marley, M. S., Saumon, D., Cushing, M., et al. 2012, ApJ, 754, 135
Marley, M. S., Saumon, D., Visscher, C., et al. 2021, ApJ, 920, 85
Mathur, S., Metcalfe, T. S., Woitaszek, M., et al. 2012, ApJ, 749, 152
Mawet, D., Milli, J., Wahhaj, Z., et al. 2014, ApJ, 792, 97
McQuillan, A., Mazeh, T., & Aigrain, S. 2014, ApJS, 211, 24
Mesa, D., D'Orazi, V., Vigan, A., et al. 2020, MNRAS, 495, 4279
Metcalfe, T. S., Creevey, O. L., Doğan, G., et al. 2014, ApJS, 214, 27
Mukherjee, S., Batalha, N. E., Fortney, J. J., & Marley, M. S. 2023, ApJ, 942, 71
Nakajima, T., Oppenheimer, B. R., Kulkarni, S. R., et al. 1995, Natur, 378, 463
Nissen, P. E., Christensen-Dalsgaard, J., Mosumgaard, J. R., et al. 2020, A&A, 640, A81
Perrin, M. D., Sivaramakrishnan, A., Lajoie, C.-P., et al. 2014, Proc. SPIE, 9143, 91433X
Pietrinferni, A., Cassisi, S., Salaris, M., & Castelli, F. 2004, ApJ, 612, 168
Pueyo, L. 2016, ApJ, 824, 117
Ricker, G. R., Winn, J. N., Vanderspek, R., et al. 2015, JATIS, 1, 014003
Rieke, M. J., Kelly, D. M., Misselt, K., et al. 2023, PASP, 135, 028001
Rosenthal, L. J., Fulton, B. J., Hirsch, L. A., et al. 2021, ApJS, 255, 8
Santos, A. R. G., Breton, S. N., Mathur, S., & García, R. A. 2021, ApJS, 255, 17
Silva Aguirre, V., Lund, M. N., Antia, H. M., et al. 2017, ApJ, 835, 173
Smith, J. C., Stumpe, M. C., Van Cleve, J. E., et al. 2012, PASP, 124, 1000
Soummer, R., Pueyo, L., & Larkin, J. 2012, ApJL, 755, L28
2013, STScI Development Teampysynphot: Synthetic photometry software package, Astrophysics Source Code Library, ascl:1303.023
Stumpe, M. C., Smith, J. C., Van Cleve, J. E., et al. 2012, PASP, 124, 985
Tayar, J., Claytor, Z. R., Huber, D., & van Saders, J. 2022, ApJ, 927, 31
Trifonov, T., Tal-Or, L., Zechmeister, M., et al. 2020, A&A, 636, A74
Ulrich, R. K. 1986, ApJL, 306, L37
Virtanen, P., Gommers, R., Oliphant, T. E., et al. 2020, NatMe, 17, 261
Vousden, W. D., Farr, W. M., & Mandel, I. 2016, MNRAS, 455, 1919
Wang, J. J., Ruffio, J.-B., De Rosa, R. J., et al. 2015, pyKLIP: PSF Subtraction for Exoplanets and Disks, Astrophysics Source Code Library, ascl:1506.001
Wood, C. M., Boyajian, T., Braun, K. v., et al. 2019, ApJ, 873, 83